Analyzing the role of copper in the soot oxidation performance of $BaMnO_3$-perovskite-based catalyst obtained by modified sol-gel synthesis

Verónica Torregrosa-Rivero, María-Salvadora Sánchez-Adsuar, and María-José Illán-Gómez*

Carbon Materials and Environment Research Group, Department of Inorganic Chemistry, Faculty of Science, University of Alicante San Vicente del Raspeig, 03690, Alicante, Spain

Abstract

A series of $BaMn_{0.7}Cu_{0.3}O_3$ solids were prepared by a modified sol-gel method in which carbon black (VULCAN XC-72R), and different calcination temperatures (BMC3-CX, where X indicates the calcination temperature) have been used. The fresh and used catalysts were characterized by ICP-OES, XRD, XPS, FESEM, TEM, O_2-TPD and H_2-TPR. The presence of a carbon black during sol-gel synthesis of BMC3 mixed oxide allows diminishing the calcination temperature needed to achieve the perovskite structure, but it hinders the formation of the $BaMnO_3$ polytype. The use of low calcination temperatures during synthesis reduces the sintering effects, and the mixed oxides present lower particle size, slightly higher BET surface areas and macropores with lower diameter than BMC3. The distribution of copper in BMC3-CX catalysts depends on the calcination temperature and copper insertion into the perovskite structure is promoted as the calcination temperature increases. All BMC3-CX catalysts are active for NO to NO_2 and NO_x-assisted soot oxidation processes, but only BMC3-C600 and BMC3-C700 show higher catalytic activity than BMC3 reference catalyst. BMC3-C600 presents the best performance as it features a high amount of surface copper and oxygen vacancies that increase during reaction. The comparison between the performance of the best catalysts of the BM-CX series (BM-C700) and of the BMC3-CX series (BMC3-C600) suggests that the unique advantage of using copper in the modified sol-gel synthesis is an additional decrease of 100ºC in the calcination temperature used for the synthesis, which is 700ºC for BM-CX and 600ºC for BMC3-CX.

Keywords: $BaMnO_3$ perovskite; diesel soot oxidation, sol-gel synthesis, carbon black, copper

* Corresponding author.

Email adresses: illan@ua.es (María-José Illán-Gómez)

1. Introduction

Due to the current demand for cheaper and more efficient technologies, perovskite-like materials (ABO_3) are being widely studied for different purposes [1-3]. The perovskites are interesting mixed oxides as their properties can be widely tuneable by using different strategies, such as i) synthesis procedure [4-8], ii) selection of A [2,3] and B [9,10] cation, iii) partial substitution of A [11,12] and/or B [13-17] cation, and iv) doping [11, 18-20]. Among other use, these solids are potential substitutes of PGM-based catalysts [21-24], highly used in the current automotive exhausts to remove the pollutants before being emitted to the atmosphere.

Previous results of the authors [25] reveal that the use of a modified sol-gel synthesis seems to improve the chemical and physical properties of the $BaMnO_3$ perovskite and, for hence, the catalytic activity for NO to NO_2 conversion and for diesel soot oxidation. The use of carbon black during sol-gel synthesis allows a decrease in the calcination temperature to obtain a perovskite-like structure from 850ºC to 600ºC and, consequently, the sintering effects decreased, and an enhanced catalytic performance is observed. On the other hand, it was demonstrated that the incorporation of copper, for the partial substitution of Mn in the $BaMnO_3$ perovskite ($BaMn_{0.7}Cu_{0.3}O_3$), improves the catalytic stability for soot oxidation during successive NO_x-TPR cycles. This fact is due to the enhancement of initial soot oxidation rate which allows a reduction in the carbon deposition and, hence, the catalyst deactivates more slowly than the copper-free perovskite ($BaMnO_3$) [26].

Therefore, the aim of this paper is to analyse the effect of the modified sol-gel synthesis (using carbon black and different calcination temperatures [25]) combined with the partial substitution of manganese by copper [26] in the chemical and physical properties of the $BaMnO_3$ perovskite. Furthermore, the catalytic activity of synthetized catalysts for NO to NO_2 conversion and, for diesel soot oxidation is also analysed.

2. Materials and Methods

2.1. Synthesis and characterization of catalysts

A series of $BaMn_{0.7}Cu_{0.3}O_3$ solids were prepared by a modified sol-gel method in which carbon black (VULCAN XC-72R), and different calcination temperatures (BMC3-CX, where X indicates the calcination temperature) have been used. As reference, a $BaMn_{0.7}Cu_{0.3}O_3$ solid was prepared by the conventional sol-gel synthesis (BMC3).

The sol-gel synthesis of BMC3 [26] starts with a citric acid solution (1M) heated up to 60ºC and a pH of 8.5, adjusted with an ammonia solution, in which the precursors ($Ba(CH_3COO)_2$, $Mn(NO_3)_2 \cdot 4 \cdot H_2O$, and $Cu(NO_3)_2 \cdot 3 \cdot H_2O$) are added. The solution is heated up to 65ºC and, after 5h, a gel is formed which is subsequently dried at 90ºC for 48h. Finally, the dried solid is calcined at 150ºC (1ºC/min) for 1h, and at 850ºC (5ºC/min) for 6h.

The modified sol-gel synthesis follows the steps of the conventional sol-gel synthesis above described but adding carbon black (Vulcan XC-72R) with a 1:1 (carbon black: $BaMn_{0.7}Cu_{0.3}O_3$) mass ratio [25]. Then, the mixture is vigorously agitated for 1 h, and after drying the mixture at 90ºC for 48h, the solid is calcined at 150ºC (1ºC/min) for 1h, and at different temperatures ranging from 600ºC to 950ºC (5ºC/min) for 6h.

For samples characterization, different techniques have been used.

The barium, manganese and copper content were measured by micro-X-Ray fluorescence (µ-XRF), using an Orbis Micro-XRF Analyzer from EDAX and by ICP-OES, on a Perkin-Elmer device model Optimal 4300 DV. For ICP-OES analysis, the elements are extracted by the mineralization of the samples using a diluted aqua regia solution (HNO_3:HCl, 1:3) and stirring at room temperature for 1 hour.

The textural properties were determined by N_2 adsorption at -196ºC using an Autosorb-6B instrument and by Hg porosimetry carried out in a Poremaster-60 GT equipment, both from Quantachrome (Anton Paar Austria GmbH). The samples were degassed at 250ºC for 4 h before the N_2 adsorption experiments and dried at 60ºC for 12 h before Hg porosimetry analysis.

The degree of removal of carbon black used in the modified sol-gel synthesis has been determined by Thermogravimetric Analysis (TGA) in a Q-600-TA equipment, by heating 10 mg of solid from room temperature to 950ºC (10ºC/min), under a flow of 100mL/min of helium.

The crystalline structure was studied by X-Ray Diffraction (XRD). The X-Ray patterns were recorded between 20-80º 2θ angles with a step rate of 0.4º/ min and using Cu Kα (0.15418 nm) radiation in a Bruker D8-Advance device.

The morphology of catalysts was analysed by electronic microscopy, using a JEOL JEM-1400 Plus TEM equipment for Transmission Electronic Microscopy (TEM), and a ZEISS Merlin VP Compact for Field Emission Scanning Electronic Microscopy (FE-SEM).

The chemical surface properties were obtained by X-Ray Photoelectron Spectroscopy (XPS), using a K-Alpha Photoelectron Spectrometer by Thermo-Scientific with an Al K$_\alpha$ (1486.7 eV) radiation source. To obtain XPS spectra, the pressure of the analysis chamber was maintained at 5×10^{-10} mbar. The binding

energy (BE) and kinetic energy (KE) scales were adjusted by setting the C 1s
transition at 284.6 eV, and the BE and KE values were then determined with the
peak-fit software of the spectrometer. The XPS ratios $O_{Lattice}/(Ba+Mn)$,
$Cu/(Ba+Mn+Cu)$ and $Mn(IV)/Mn(III)$ have been calculated by the area under the
suggested deconvolutions of O1s, Mn $3p^{3/2}$, Cu $2p^{3/2}$ and Ba $3d^{5/2}$ bands.

Reducibility of catalysts was determined by Temperature Programmed
Reduction with H_2 (H_2-TPR) in a Pulse Chemisorb 2705 (from Micromeritics) with a
Thermal Conductivity Detector (TCD) and using 30 mg of sample which was heated
at 10ºC/min from 25ºC to 1000ºC in 5%H_2/Ar atmosphere (40 mL/min). The
quantification of the H_2 consumption was carried out using a CuO reference sample.

O$_2$-TPD experiments were performed in a TG-MS (Q-600-TA and Thermostar
from Balzers Instruments (Pfeiffer Vacuum GmbH, Germany) respectively), with 16
mg of sample heated at 5ºC/min from room temperature to 900ºC under a 100
mL/min of helium atmosphere. The 18, 28, 32 and 44 m/z signals were followed for
H_2O, CO, O_2 and CO_2 (respectively) evolved during these experiments. The amount
of evolved oxygen is estimated using a CuO reference sample.

2.2. Activity tests

The activity for NO and NO$_x$-assisted soot oxidation was carried out by
Temperature Programmed Reaction in a quartz fixed-bed reactor, heated up from
25ºC to 800ºC (10ºC/min), under a gas flow mixture (500 mL/min) containing 500
ppm NOx, 5% O_2, balanced with N_2. For NO oxidation experiments, 80 mg of
catalyst was diluted with 320 mg SiC. Soot oxidation tests were performed mixing
80 mg of catalyst and 20 mg of Printex-U (the carbon black used as model soot) with
a spatula to ensure loose contact, and the mixture was diluted with 300 mg of SiC.
The most active catalysts were also tested under isothermal soot oxidation
conditions, at 450ºC for 180 min. The gas composition was monitored by specific
NDIR-UV gas analysers for NO, NO_2, CO, CO_2 and O_2 (Rosemount Analytical
Model BINOS 1001, 1004 and 100, Emerson Electric Co., St. Louis, MO, USA).The
NO$_x$ conversion and the NO_2 generation percentages were calculated using the
following equations:

$$NO_x \text{ conversion}(\%) = \frac{(NO_{x,in} - NO_{x,out})}{NO_{x,in}} \cdot 100 \quad (1)$$

$$NO_{2,out}/NO_{x,out}(\%) = \frac{NO_{2,out}}{NO_{x,out}} \cdot 100 \quad (2)$$

Where $NO_{2, out}$ and $NO_{x,out}$ are the NO_2 and NO$_x$ (NO+NO_2) concentrations
measured at the reactor exit.

The soot conversion and CO_2 selectivity were determined as:

$$\text{Soot conversion (\%)} = \frac{\sum_0^t CO_2 + CO}{\sum_0^{final}(CO_2 + CO)} \cdot 100 \qquad (3)$$

$$\text{CO}_2 \text{ Selectivity (\%)} = \frac{CO_2}{\sum_0^{final}(CO_2 + CO)} \cdot 100 \qquad (4)$$

Where $\sum_0^t(CO_2 + CO)$ is the amount of CO_2 and CO evolved at a time t, while $\sum_0^{final}CO_2$ and $\sum_0^{final}(CO_2 + CO)$ are the total amount of CO_2 and $CO+CO_2$ evolved during the test.

3. Results and Discussion

3.1. Characterization of fresh catalysts

The remaining carbon black after the calcination step was determined by thermogravimetric analysis. The weight profiles for BMC3-CX series (shown in Figure A.1 in the Appendix A), indicate that, as observed in the absence of copper [25], most of the carbon black has been efficiently removed during the synthesis as the percentage of remaining carbon black ranges from 6% for BMC3-C600 to 1% for BMC3-C850 (see data in Table A.1 in the Appendix A).

3.1.1. Chemical composition: ICP-OES

The copper, manganese and barium content has been determined by ICP-OES and the results are shown in Table 1 as the mass percentage of copper and the Cu/Ba and Mn/Ba molar ratios, being the nominal values corresponding to the $BaMn_{0.7}Cu_{0.3}O_3$ composition included as a reference. The results point out that the modified sol-gel synthesis is a successful method to obtain the $BaMn_{0.7}Cu_{0.3}O_3$ composition since all the catalysts present not only the required amount of copper, but also copper and manganese are in the expected molar ratios respect to barium.

Table 1. Copper content (w/w%), Cu/Ba and Mn/Ba molar ratio determined by ICP-OES for BMC3 series and BMC3 as reference

	Cu (%)	Cu/Ba	Mn/Ba
Nominal[a]	7.8	0.3	0.7
BMC3-C600	8.0	0.3	0.7
BMC3-C700	7.6	0.3	0.7
BMC3-C750	7.3	0.3	0.7

BMC3-C850	8.0	0.3	0.7
BMC3	7.6	0.3	0.7

3.1.2. Structural properties: XRD

Figure 1 gathers X-Ray patterns for BMC3-CX series and for BM ($BaMnO_3$) and BMC3 as references [26]. As observed for BM-CX catalysts series [25], the use of carbon black allows the synthesis of perovskite-like mixed oxides ($BaMnO_3$ hexagonal PDF number: 026-0168, denoted by the ICDD) at lower temperatures than the conventional sol-gel method [26]. Additionally, it is observed that the formation of the $BaMnO_3$ polytype, the main crystal phase in BMC3 [26], is hindered in presence of carbon black.

The X-Ray pattern of BMC3 [26] reveals that the insertion of copper into the $BaMnO_3$ perovskite-like structure, by partial substitution of manganese, promotes a new order in MnO_6 octahedrons, forming a $BaMnO_3$ hexagonal polytype due to the difference in the ionic radii of manganese (Mn^{4+}=53 pm, Mn^{3+}=65 pm) and copper (Cu^{2+}=73 pm) with octahedral coordination [27]. Nevertheless, in presence of the carbon black, the $BaMnO_3$ polytype structure is not the main phase and a mixture of $BaMnO_3$ hexagonal and polytype phases is identified. In fact, a relationship between the calcination temperature and the proportion of each crystalline phase is observed, because as the calcination temperature increases, the polytype phase becomes more relevant, being the main phase for BMC3-C750 and BMC3-C850. Thus, to try obtaining a pure $BaMnO_3$ polytype crystal phase, a higher calcination temperature was used (950ºC), but for BMC3-C950 sample a low amount of $BaMnO_3$ hexagonal phase is still being identified. So, it can be concluded that carbon black hinders the insertion of copper, but the blocking effect decreases as the calcination temperature increases.

167
168
169
170
171
172
173
174
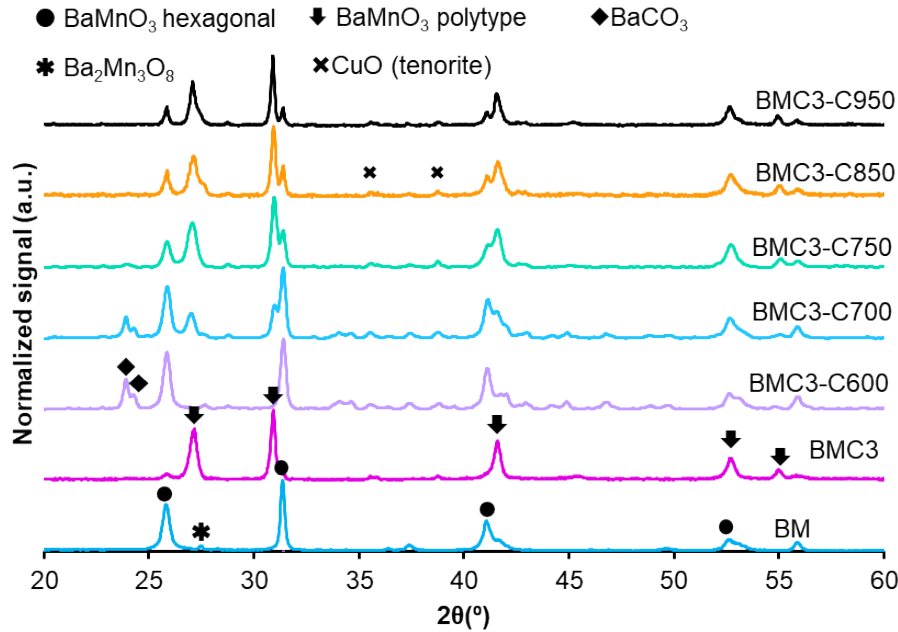175
176
177
178
179
180
181
182
183
184
185
186
187
188

Figure 1. X-ray patterns for BMC3-CX series and BM and BMC3 as references [26]

On the other hand, even all the catalysts of the BMC3-CX series present almost the same percentage of copper (see Table 1), the diffraction peaks corresponding to CuO (pointed with a cross in Figure 1) do not become more intense as the calcination temperature decreases, as it could be expected if copper is not inserted into the perovskite lattice [14, 28]. Table 2 presents the lattice parameters for the two structures detected. The lattice parameters corresponding to $BaMnO_3$ hexagonal structure do not change, therefore, this structure is not modified due to the presence of copper. However, attending to the $BaMnO_3$ polytype lattice parameters, it is found that, as the calcination temperature increases, the lattice parameters are closer to the observed for BMC3 [26]. So, this trend confirms that the insertion of copper into the perovskite structure needs high temperatures.

Thus, the X-Ray pattern of BMC3-C600 reveals that copper is not being inserted into the lattice, because the unique perovskite phase is $BaMnO_3$ hexagonal and the lattice parameters are very similar to the shown by BM, which presents the $BaMnO_3$ hexagonal structure. However, the $CuO/BaMnO_3$ intensity does not increase regarding the others BMC3-CX catalysts. Therefore, it seems that copper oxide seems to be well dispersed, and the crystal size is lower than the detection limit of the DRX technique or it could be forming amorphous particles of CuO.

As for BM-CX catalysts [25], different crystal phases are identified for the BMC3-CX catalyst series depending on the calcination temperatures used during synthesis:

BMC3-C600 and BMC3-C700 catalysts show the $BaMnO_3$ hexagonal structure as the main phase, being barium carbonate, which is present due to the low calcination temperature [29], and copper oxide the minority crystal phases.

BMC3-C750 and BMC3-C850 also present the BaMnO$_3$ hexagonal structure as the main phase, but barium carbonate is not detected (since the calcination temperature is high enough to remove it) and the polytype and a low amount of copper oxide are identified.

Table 2. Structural, morphological and textural data for BMC3-CX series and BM and BMC3 as references

| | Average crystal size (nm) | | Lattice parameters | | | | S$_{BET}$ (m^2/g) |
| | | | BaMnO$_3$[c] | | Polytype[d] | | |
	BaMnO$_3$[a]	polytype[b]	a (nm)	c (nm)	a (nm)	c (nm)	
BMC3-C600	27	-	5.693	4.809	-	-	23
BMC3-C700	26	-	5.697	4.806	5.769	4.395	25
BMC3-C750	-	26	5.697	4.799	5.769	4.378	9
BMC3-C850	-	29	5.697	4.806	5.776	4.**357**	4
BMC3	-	21	-	-	5.789	4.355	<5
BM	40	-	5.698	4.806	-	-	5

[a] main diffraction peak BaMnO$_3$ hexagonal (≈31.4º)

[b] main diffraction peak BaMnO$_3$ polytype (≈30.9º)

[c] from main diffraction peaks BaMnO$_3$ hexagonal ≈31.4º (110) y ≈25.8º (101)

[d] from main diffraction peaks BaMnO$_3$ hexagonal ≈30.9º (110) y ≈27.0º (101).

BMC3-C950 shows the BaMnO$_3$ polytype structure as the main crystal phase but the hexagonal phase is still detected. So, calcination temperatures higher than 950ºC should be used to achieve the pure phase detected in BMC3 [26].

The average crystal sizes, calculated by the Scherrer equation for both perovskite phases, shown in Table 1, are lower than calculated for BM reference catalyst [25] but do not reveal a clear trend with the calcination temperature. Therefore, the presence of copper seems to hinder the crystal growth, since all the BMC3-CX present similar average crystal sizes. A similar effect has been observed for magnesium dopped LaCoO$_3$ perovskites [30, 31].

Thus, the XRD results suggests that for BMC3-CX catalysts series, the incorporation of copper into the perovskite-like structure (BaMnO$_3$ hexagonal) depends on the calcination temperature: at 600ºC, the formation of small particles of copper oxide seems to be promoted, and at temperatures higher than 700ºC, the diffusion of copper into the perovskite-like lattice is facilitated, allowing the formation of the BaMnO$_3$ polytype phase.

223
224
225
226
227
228
229
230
231
232
233
234
235
236
237

3.1.3. Textural and morphological properties

The low BET surface area of samples, featured in Table 2, are the expected for solids with a poorly developed porosity, as mixed oxides with perovskite like structure are [33-35]. However, as for BM-CX series [25], a slight increase in the BET surface area as the calcination temperature decreases is found. This fact seems to be related to the lower trend of the particles to aggregate revealed by TEM images, shown in Figure 2, where amorphous particles with different sizes are observed [25].
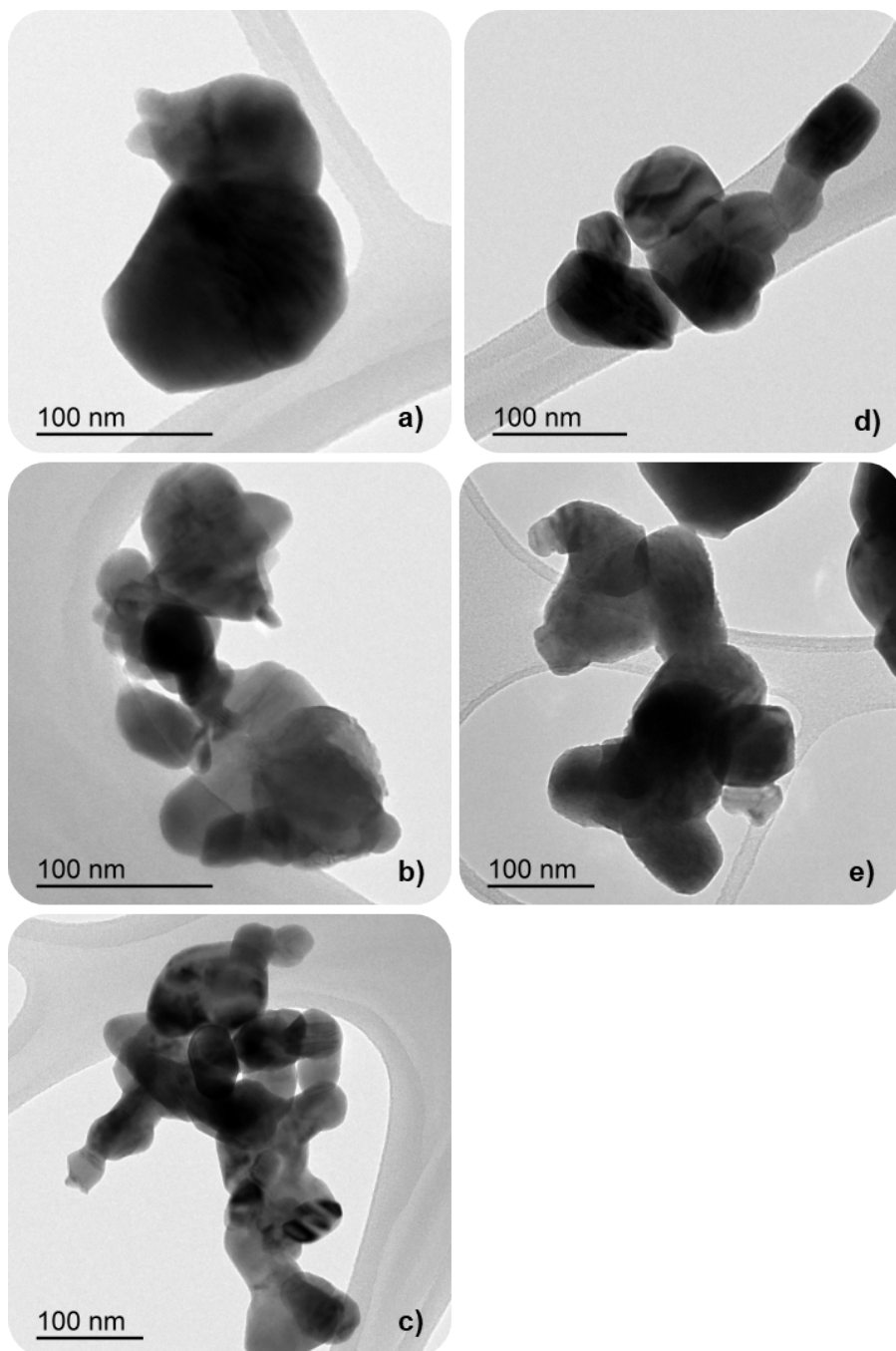
Figure 2. TEM images for catalyst: (a) BMC3, (b) BMC3-C600, (c) BMC3-C700, (d) BMC3-C750 and (e) BMC3-C850

The range of pore diameter has been estimated by Hg porosimetry and Figure 3 shows the logarithmic pore size distribution for the BMC3-CX series and BMC3 reference catalyst. It is observed that the decrease of the calcination temperature in the presence of the carbon black allows the development of a narrower macroporosity, so, lower pore diameter than BMC3 reference is found for BMC3-CXseries as the calcination temperature decreases. This effect was also observed in the absence of copper [25] and for perovskite-like solids when PMMA is used as

hard-template [36,37]. Thus, while BMC3 mainly presents large-diameter   255
macropores related to the inter-particle space, BMC3-C600 shows a combination of   256
macropores due to the intra and inter-particle space. Thus, it seems to be confirmed   257
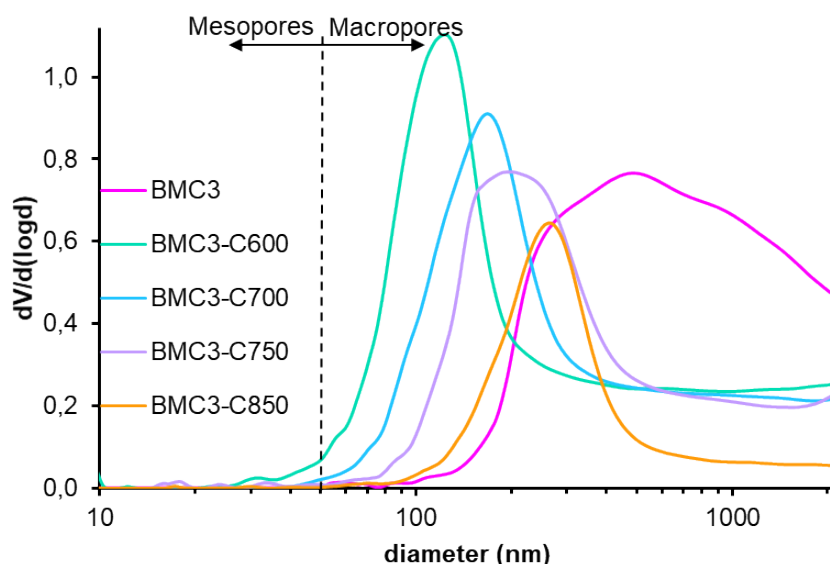that the use of carbon-black is effective to create intra-particle porosity.   258

Figure 3. Logarithmic pore diameter for BMC3-CX series and BMC3 as reference   259

In conclusion, the use of carbon black during sol-gel synthesis of BMC3: i)   260
hinders the insertion of copper into the perovskite lattice, ii) allows reducing the   261
calcination temperature needed to achieve a perovskite-like structure and, iii)   262
diminishes the sintering effects at low calcination temperature, promoting an   263
enhanced macroporosity [25, 6,37].   264

3.1.3. Surface composition: XPS   265

Figure 4.a shows the XPS spectra of Cu $2p^{3/2}$ transition, where the experimental   266
data (black dots) have been included to feature the accuracy of the envelope profile   267
(continuous line), and consequently, of the deconvolutions. The spectra indicate that   268
copper is present as Cu (II) in all catalysts since a maximum over 933 eV and the   269
shake-up satellite peaks at 941 eV and 944 eV are detected [38,39]. Moreover, the   270
Wagner plot (Figure 4.b), which includes some references from the NIST X-Ray   271
Photoelectron Spectroscopy data base [40], proves that Cu(I) is not presents on the   272
catalysts surface. However, the deconvolution of Cu(II) signal points out two   273
different contributions corresponding to two degrees of interaction with the   274
perovskite [26]: i) the signal at the highest binding energy, 935 eV, assigned to a   275
copper with a strong interaction with the perovskite, and ii) the signal at the lowest   276
binding energy, 933.5 eV, corresponding to a copper with a weak interaction with   277
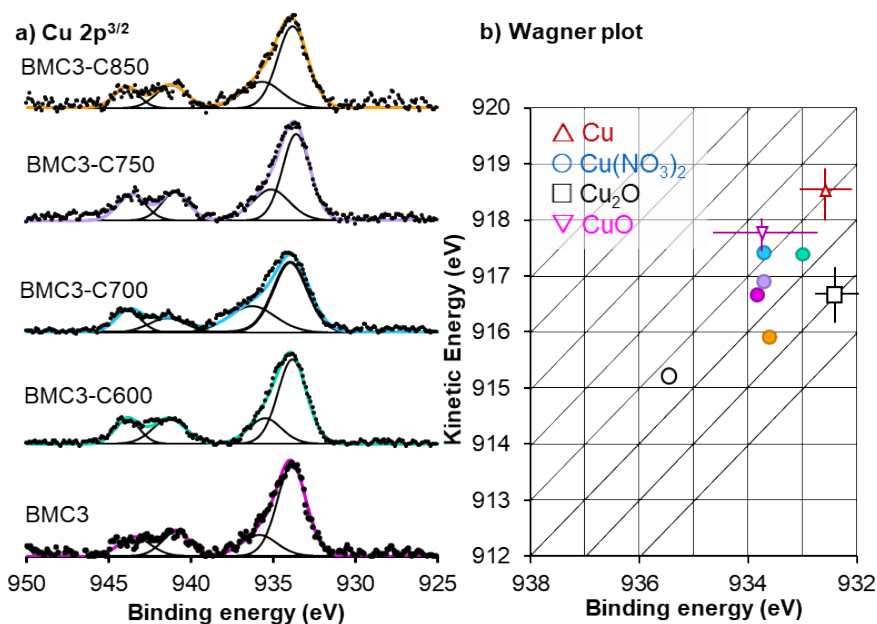the perovskite [41,42].   278

279

Figure 4. (a) XPS spectra of Cu 2p$^{3/2}$ transition for BMC3-CX series and BMC3 as reference. (b) Wagner Plot with reference data from NIST X-ray Photoelectron Spectroscopy Database. Experimental data: BMC3 (pink dot), BMC3-C600 (green dot), BMC3-C750 (blue dot) and BMC3-C850 (orange dot)
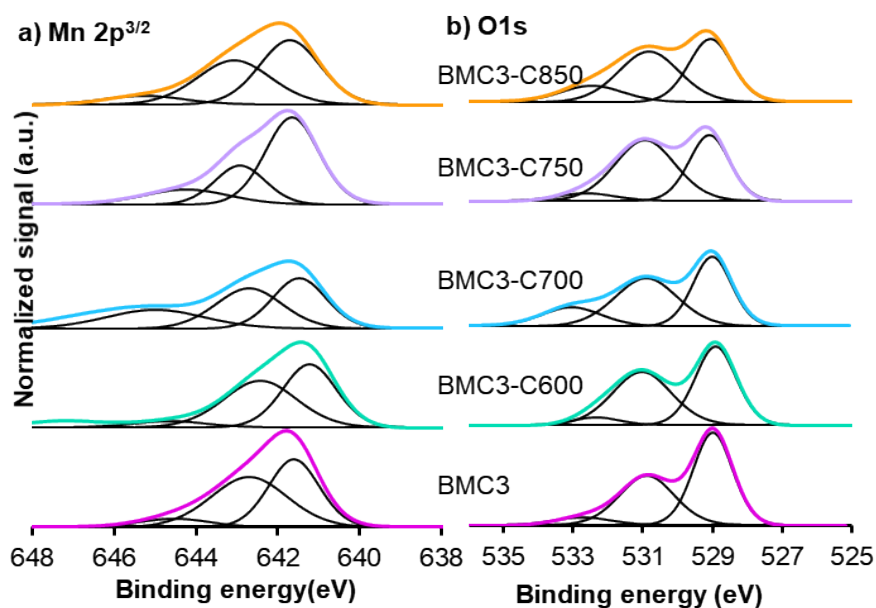

Figure 5. XPS spectra of (a) O1s, and (b) Mn 2p$^{3/2}$ transitions for BMC3-CX series and BMC3 as reference

Figure 5 shows the XPS spectra of oxygen (O1s transition) and manganese (Mn2p$^{3/2}$ transition). The profiles for Mn (due to the presence of the Mn (III) satellite peak at 645 eV and the signal over 643 eV linked to Mn(IV) [9,43]) confirm that Mn(III) and Mn(IV) coexist on the catalysts surface, as observed for BM-CX series [25]. The Mn(IV)/Mn(III) ratio (included in Table 3) points out Mn(III) as the main

oxidation state in all catalysts, except in BMC3-C600 catalyst which presents both oxidation states in a similar proportion.

Table 3. XPS ratios and β-O_2 evolved during O_2-TPD experiments for BMC3-CX series and BMC3 as reference

	$O_{Lattice}/$ (Ba+Mn+Cu)	Mn(IV)/Mn(III)	Cu/ (Ba+Mn+Cu)	β-O_2 ($\mu mol/g_{cat}$)
Nominal	1.5 [a]	-	0.15 [a]	-
BMC3-C600	1.0	0.9	0.15	215
BMC3-C700	1.1	0.6	0.13	220
BMC3-C750	1.0	0.5	0.13	203
BMC3-C850	1.1	0.6	0.09	173
BMC3	1.3	0.6	0.12	205

[a] calculated for $BaMn_{0.7}Cu_{0.3}O_3$ composition

The O1s spectra show three contributions corresponding to three oxygen species: lattice oxygen ($O_{Lattice}$, at ca. 529 eV), surface groups (ca. 531 eV) and oxygen from adsorbed water (ca. 533 eV) [44-47]. In general terms, the catalysts present an almost similar distribution of oxygen species.

Using the area under the peaks corresponding to the different elements, the Cu/(Ba+Mn+Cu) ratio is calculated for BMC3-CX series and the results are included in Table 3. In general terms, the values are not far from the nominal one, 0.15 for $BaMn_{0.7}Cu_{0.3}O_3$ composition, being higher than the obtained for BMC3 reference, in which copper is inserted into the lattice. However, the Cu/(Ba+Mn+Cu) ratio diminishes as the calcination temperature increases, so, it seems that the use of high calcination temperatures facilitates the copper diffusion through the lattice and, consequently, the insertion into the perovskite structure forming the $BaMnO_3$ polytype. In fact, for BMC3-C850, the Cu/Ba+Mn+Cu ratio is lower than the nominal one, confirming that the copper insertion is easier as the calcination temperature increases. The $O_{Lattice}$ /Ba+Mn+Cu ratio has been also calculated and included in Table.3. As the values are lower than the nominal one (1.5), the presence of surface oxygen defects (as oxygen vacancies [47]) are detected. These vacancies must be formed to compensate the positive charge defect due to the presence of Cu(II) and Mn(III) on surface. All the BMC3-CX catalysts show a lower value than the corresponding to BMC3·reference, so, larger amount of oxygen defects/vacancies are formed. However, the $O_{Lattice}$/Ba+Mn+Cu ratio is not significantly affected by the calcination temperature.

Finally, note that the Cu/Ba+Mn+Cu ratio for BMC3-C600 (in which the BaMnO$_3$ polytype phase is not detected) corresponds to the nominal value (0.15), suggesting that copper should be homogeneously distributed and well-dispersed on the surface. BMC3-C600 also presents the highest amount of Mn(IV) on surface, probably formed by oxidation of Mn(III) to compensate the defect of positive charge due to the presence of Cu(II), which additionally causes an increase in the amount of oxygen vacancies on surface [48-50] respect to BMC3 reference. In summary, BMC3-C600 presents the most homogeneously copper distribution and the highest amount of Mn (IV) and surface oxygen vacancies.

3.1.4. Reducibility: H$_2$-TPR

To study the reducibility of the catalysts, Temperature Programmed Reduction in hydrogen experiments (H$_2$-TPR) have been carried out and Figure 6 shows the hydrogen consumption profiles. A synergetic effect between copper and manganese is observed as both species are reduced at a temperature (about 250ºC) lower than the respective references (CuO and BM). The boosted reducibility of BMC3-C600 could be related to the smaller particles formed since the low calcination temperature used for its synthesis seems to minize the sintering effects. Therefore, smaller crystal size is obtained for this sample, and the boundary grains increase, in which the copper species are more reducible[50–52].
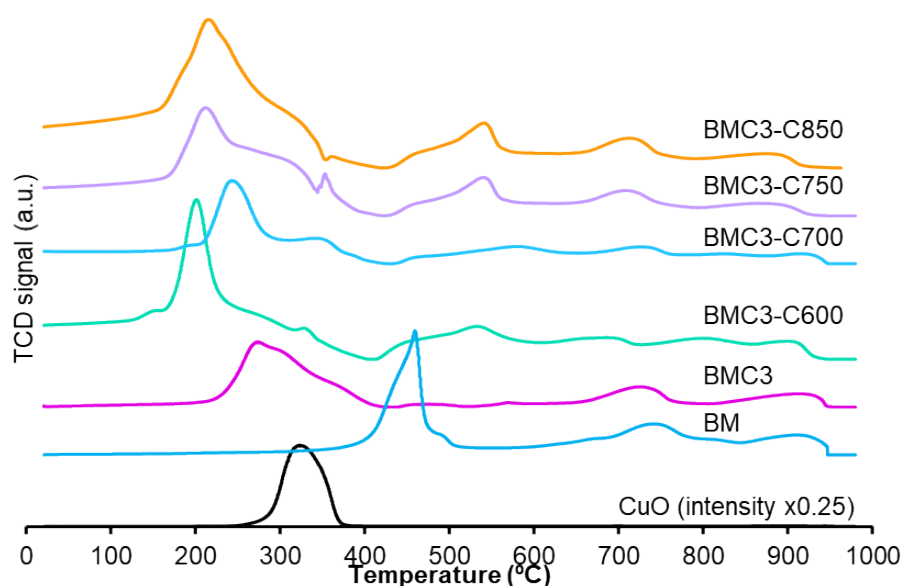

Figure 6. Hydrogen consumption profiles in TPR conditions for BMC3-CX series and BM, BMC3 and CuO as references

BMC3-C600 and BMC3-C700 show a shoulder around 200ºC that could correspond to the reduction to Cu(I) of the CuO surface nanoparticles [54,55], which are presumably present based on DRX and XPS data and supported by the absence of BaMnO$_3$ polytype phase for the former and by the lowest proportion of the

polytype phase for the later. These copper species seem to present a strong
interaction with the perovskite and, as consequence, a synergetic effect is expected,
so, manganese and copper reducibility will be simultaneously improved.

The experimental hydrogen consumption per gram of catalyst has been estimated
for the region between 150ºC and 500ºC of the H_2 consumption profiles shown in
Figure 6. These values are plotted in Figure 7 regarding the nominal values
assuming the total reduction of manganese, which has been considered as pure
Mn(III) or Mn(IV) and copper as Cu(II). In Figure 7, if the experimental values are
close to the maximum values (red points), it means that Mn(IV) is the main
oxidation state, but if the values are close to the minimum ones (green points) it
points out that Mn(III) is the predominant oxidation state or that the reduction of
manganese and copper is not completed. All BMC3-CX catalysts show the
coexistence of Mn(III) and Mn(IV) oxidation states but the low value for BMC3-C700
could point out that Mn(III) is the main oxidation state or that this sample presents
the lowest reducibility. Therefore, except for the catalyst obtained at 700ºC, the
calcination temperature seems to not significantly affect the Mn(IV)/Mn(III) bulk
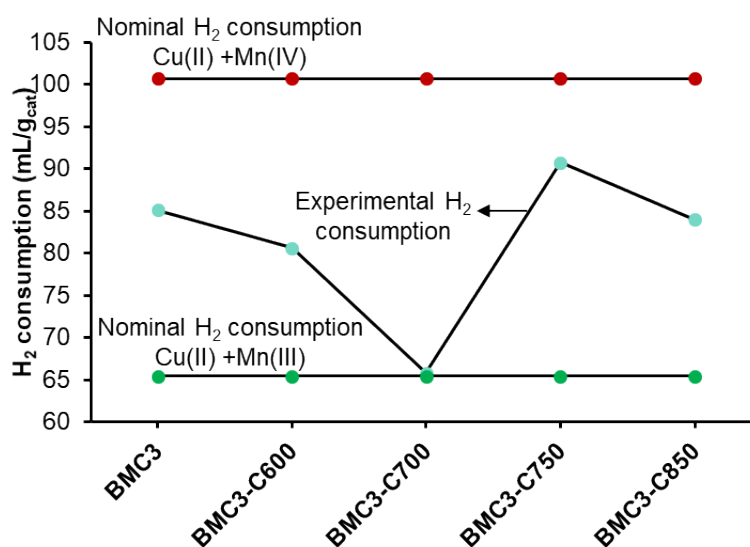proportion, as it is also revealed by XPS data for the surface.

Figure 7. Hydrogen consumption between 150ºC-500ºC corresponding to copper
and manganese reduction

    Finally, note that the hydrogen consumption at temperatures higher than 500ºC
corresponds with several reduction processes: i) at 550ºC the consumption is related
with the presence of remaining carbon black, as it was previously observed for BM-
CX series [25]; ii) at 750ºC the oxygen surface groups decompose; and iii) over
950ºC, the Mn(III) bulk to Mn(II) reduction occurs [34, 56,57].

3.1.5. Oxygen desorption: O_2-TPD

Figure 8 shows the profiles of oxygen evolved from BMC3-CX catalysts series
and from BMC3 reference catalyst during Temperature Programmed Desorption
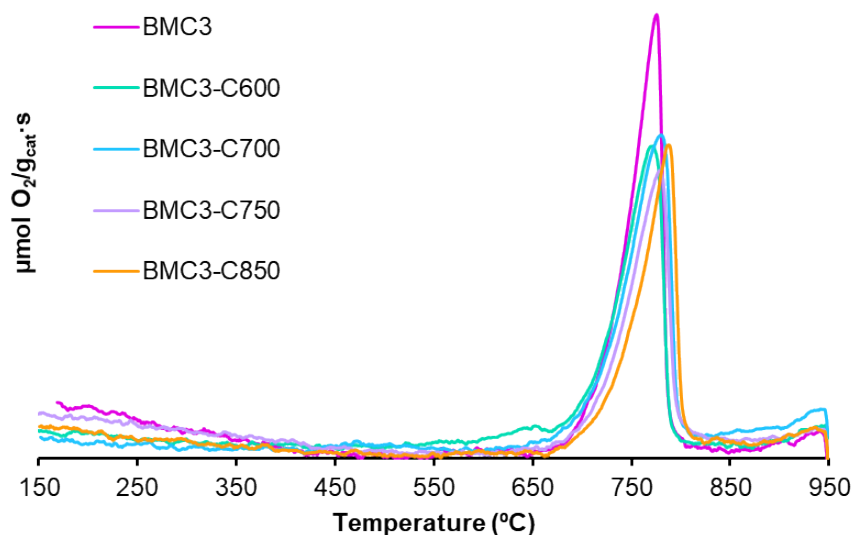experiments, being the amount of oxygen emitted included in Table 3.

Figure 8. O_2-TPD profiles for BMC3-CX series and BMC3 as reference

All catalysts mainly evolve oxygen at high temperatures (<700ºC), named β-O_2,
which comes from the perovskite lattice, and it is related with the Mn(IV) to Mn(III)
reduction and with the presence of oxygen defects that facilitate the desorption.
Both characteristics boost the lattice oxygen mobility through the lattice, and,
consequently, the reduction ability [58-60]. The O_2-TPD experiments reveal that, as
observed for BM-CX series [25], the use of carbon black during the synthesis and/or
the calcination temperature seems to not significantly affect the oxygen bulk
mobility of BMC3-CX catalysts.

3.2. Activity tests

The BMC3-CX catalysts series has been tested for two oxidation processes: i) NO
to NO_2 oxidation and ii) NO_x-assisted diesel soot oxidation. Firstly, the activity for
NO to NO_2 oxidation has been determined and then, the most active catalysts have
been used for NO_x-assisted diesel soot oxidation.

3.2.1. NO to NO_2 oxidation.

NO_x-TPR tests are useful to determine the catalytic activity for NO_x
adsorption/desorption process (Figure 9) and NO to NO_2 oxidation (Figure 10). In
Figure 9, the NO_x conversion profiles reveal that the BMC3-CX catalysts calcined at
low temperatures (between 600ºC and 750ºC) show some adsorption/desorption

capacity, which is low if it is compared with the corresponding to active catalysts for NO$_x$ storage, as Ba$_{1-y}$A$_y$Ti$_{1-x}$Cu$_x$O$_3$ [63,64], BaFeO$_3$ [65] or La$_{1-y}$A$_y$CoO$_3$ [66]. Although the NO$_x$ adsorption capacity is low, it must be considered that, for the BMC3-C600, BMC3-C700 and BMC3-C750 samples, the NO$_2$ generation profiles (Figure 10) do not show the total amount of the generated NO$_2$, it only shows the not adsorbed one. Therefore, these three samples should present a higher NO oxidation activity than BMC3 reference since they seem to adsorb more NO$_x$ than BMC3. As observed for BM-CX catalysts series [25], this performance seems to be associated to the presence of barium carbonate (detected by XRD), which is an active species for NO$_x$ adsorption [29, 65, 67-70], when the calcination temperature is under 750ºC. This fact is consistent with the crystal phases identified for BMC3-CX, since BMC3-C600 (obtained at the lowest calcination temperature), shows the highest proportion of barium carbonate and presents the highest NO$_x$ adsorption-desorption capacity; while BMC3-C950 (calcined at the highest temperature) does not show a significant NO$_x$ adsorption-desorption capacity. In fact, in a second consecutive NO$_x$-TPR cycle (not shown), the catalysts have lost their NOx adsorption-desorption capacity because the barium carbonate was decomposed during the first TPR test.
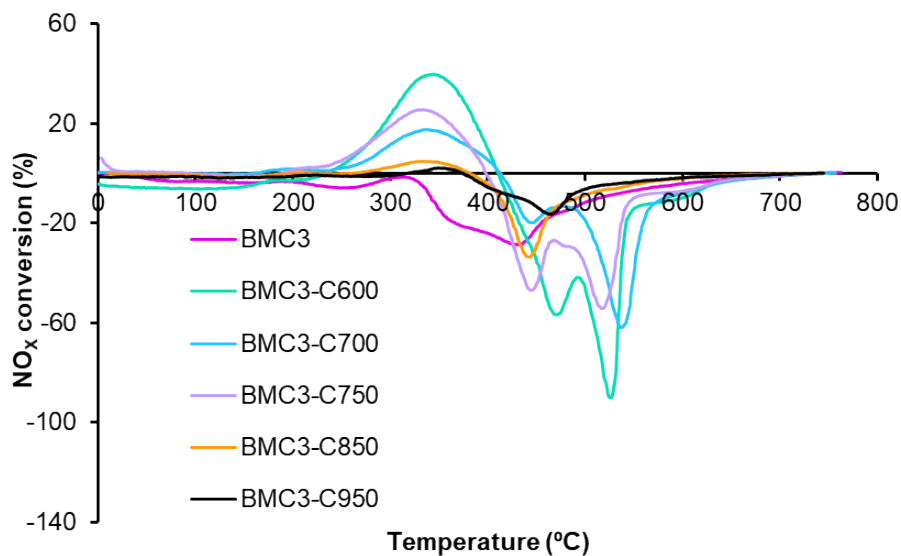

Figure 9. NO$_x$ conversion in NO$_x$-TPR conditions for BMC3-CX series and BMC3 as references
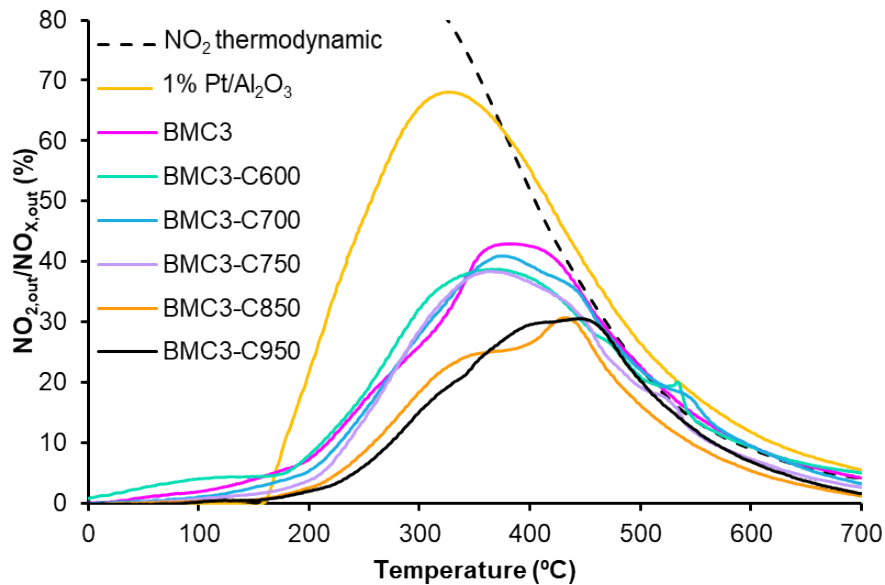
Figure 10. NO$_2$ emission profiles in NO$_x$-TPR conditions for BMC3-CX series and BMC3 and 1%Pt/Al$_2$O$_3$ as references

In Figure 10, it is observed that all BMC3-CX catalysts are active for NO to NO$_2$ oxidation under 450ºC, being the calcination temperature relevant because, while BMC3-C600, BMC3-C700 and BMC3-C750 samples show a similar performance than BMC3 reference, the catalysts calcined at the two highest temperatures (BMC3-C850 and BMC3-C950), present a lower activity. This trend could be related to sintering effects that decrease the active sites for oxidation reactions. This effect is also observed for other perovskite-based catalysts [25, 53, 61,62], if the calcination temperature required to obtain the perovskite phase is exceeded.

3.2.2. NO$_x$-assisted diesel soot oxidation

As the catalysts obtained at calcination temperatures lower than 850ºC show an acceptable NO oxidation performance, the NO$_x$-assisted soot oxidation activity has been determined for BMC3-C600, BMC3-C700 and BMC3-C750.

Figure 11 gathers the soot conversion profiles for the catalysts obtained during NO$_x$-TPR experiments in presence of model soot (PRINTEX-U), including the profiles for BMC3 and 1% Pt/Al$_2$O$_3$ as references. The three BMC3-CX samples catalyze the process, since the soot oxidation takes place at lower temperatures than in the absence of catalyst (denoted as blank). Note that BMC3-C600 presents the highest increase in the catalytic activity regarding BMC3 reference, which is close to the observed for platinum-based catalyst, and, that the activity decreases as the calcination temperature increases, being the catalytic activity of BMC3-C750 very similar to the observed for BMC3. Identical effect of calcination temperature on catalytic activity was observed by Y. Gao et al for BaMnO$_3$ perovskite [52].The

characterization results reveal that the presence of copper during the synthesis   438
minimizes the growth of crystallite (see Table 2) and that, at low calcination   439
temperatures, the insertion of copper into the perovskite structure is hindered and,   440
consequently, the formation of the $BaMnO_3$ polytype phase. Considering the copper   441
distribution, the soot oxidation profiles in NO_x-TPR conditions suggest that the   442
catalytic activity is increased if copper is not inserted into the perovskite-like lattice.   443
In this sense, F.E. López-Suárez et al, found that the role of copper species depends   444
on their location into the $SrTiO_3$ and $MgTiO_3$ perovskite-like mixed oxides [42]: the   445
CuO on surface is an active site for reduction and oxidation processes, but the lattice   446
copper is not directly involved as an active site. Thus, in BMC3-CX series the soot   447
oxidation profiles suggest that BMC3-C600 and BMC3-700 should present CuO on   448
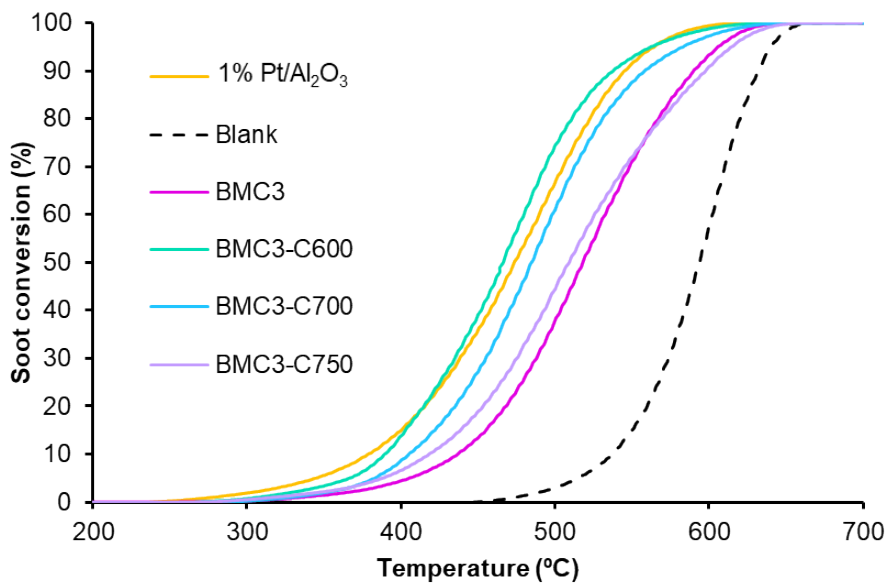surface that allows the increase in the catalytic activity.   449

Figure 11. Soot conversion profiles, in NO_X-TPR conditions for BMC3-CX series and   450
BMC3 and $1\%Pt/Al_2O_3$ as references   451

Figure 12 shows the NO_2 emission profiles during soot oxidation in NO_x-TPR   452
conditions. The difference between the NO_2 emission profiles in the absence and   453
presence of soot (Figure 9 and Figure 12, respectively) probes that a fraction of NO_2 454
is being used in the soot oxidation process. Moreover, as it has been observed for   455
BM-CX catalysts [25], BMC3-CX catalysts are active in the temperature range of   456
interest for practical applications [71], also showing a high CO_2 selectivity (above   457
95%) during the NO_x-TPR soot oxidation, as manganites are highly active for CO to   458
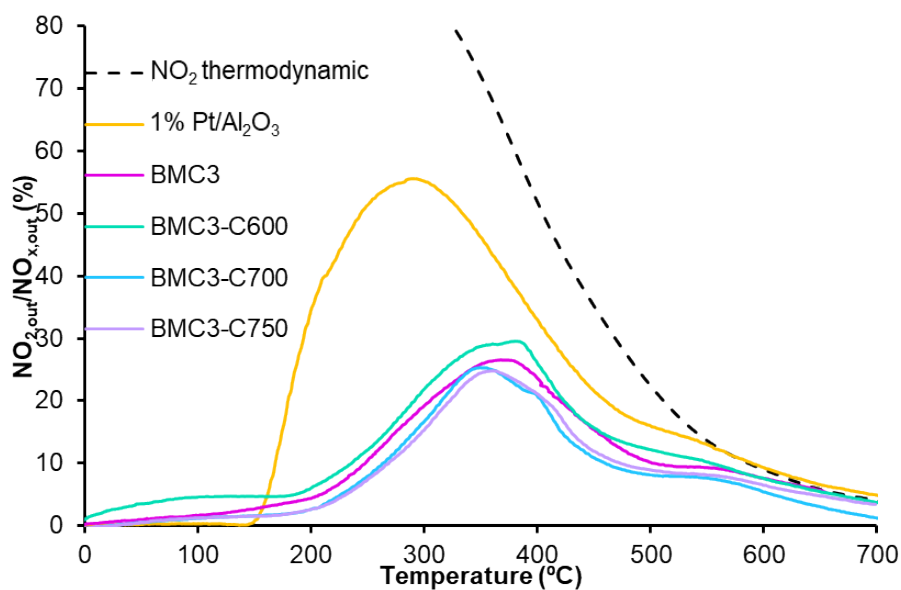CO_2 oxidation [52, 59, 72, 73].   459
    460

Figure 12. NO$_2$ emission profiles during soot oxidation in NO$_x$-TPR conditions for BMC3-CX series and BMC3 and 1%Pt/Al$_2$O$_3$ as references
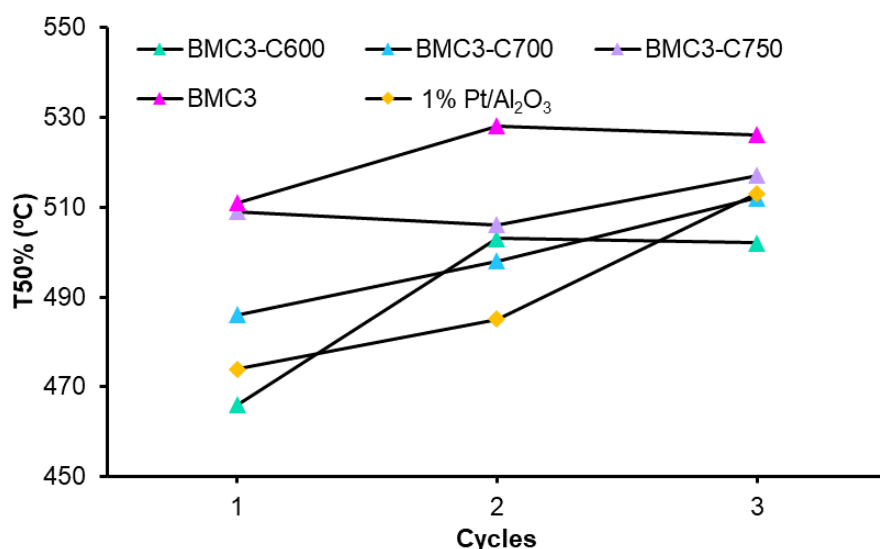
461
462

Figure 13. T50% values for BMC3-CX series and BMC3 and 1%Pt/Al$_2$O$_3$ as references during consecutive NO$_x$-TPR cycles

463
464

In order to study the stability of the catalysts, cyclic NO$_x$-TPR experiments in the presence of soot have been carried out. The selected parameter for comparative purposes is the T50% values (the temperature to achieve 50% conversion), that have been compared in Figure 13.

465
466
467
468

BMC3-C600 presents the lowest T50% value for the first cycle, but a significant increase is observed for the second cycle as consequence of the barium carbonate decomposition during the first cycle. However, the T50% value remains stable after the second cycle, pointing out a better stability than the observed for BMC3-C700

469
470
471
472

and BMC3-C750 catalysts. Comparing with BMC3 reference, BMC3-C600 shows a 473
similar performance, but it is more active because T50% values are lower. Respect to 474
the platinum-based reference catalyst (1% Pt/Al_2O_3), BMC3-C600 is slightly more 475
active after three consecutive cycles because the continuous deactivation suffered by 476
platinum catalyst, probably, due to sintering and or/oxidation effects [25,74]. 477

The results reveal that BMC3-C600 shows the best catalytic performance 478
regarding BMC3 reference because it presents the lowest T50% value and the 479
highest stability during three consecutive NO_x-TPR cycles. The physical and 480
chemical properties shown by this catalyst (a high proportion of surface copper and 481
surface oxygen vacancies, high Mn(IV)/Mn(III) ratio and high reducibility) seem to 482
justify the observed catalytic performance. In fact, several studies consider these 483
properties as key factors for NO_x-assisted soot oxidation [50, 75-78]. In addition, a 484
high CO_2 selectivity is shown during the NO_x-TPR cycles. 485

In order to study the catalytic performance for soot combustion at temperatures 486
in the range of interest for a diesel particulate filter, two consecutive isothermal 487
experiments at 450ºC have been carried out. Figure 15 shows the soot conversion 488
profiles corresponding to two isothermal reaction cycles for BMC3-C600 catalyst 489
and, for comparative purpose, for the first cycle of BMC3 and the platinum-based 490
catalyst used as references. In Table 4, the initial soot oxidation rates (calculated 491
from the slope of soot conversion profiles during the first 20 minutes of the 492
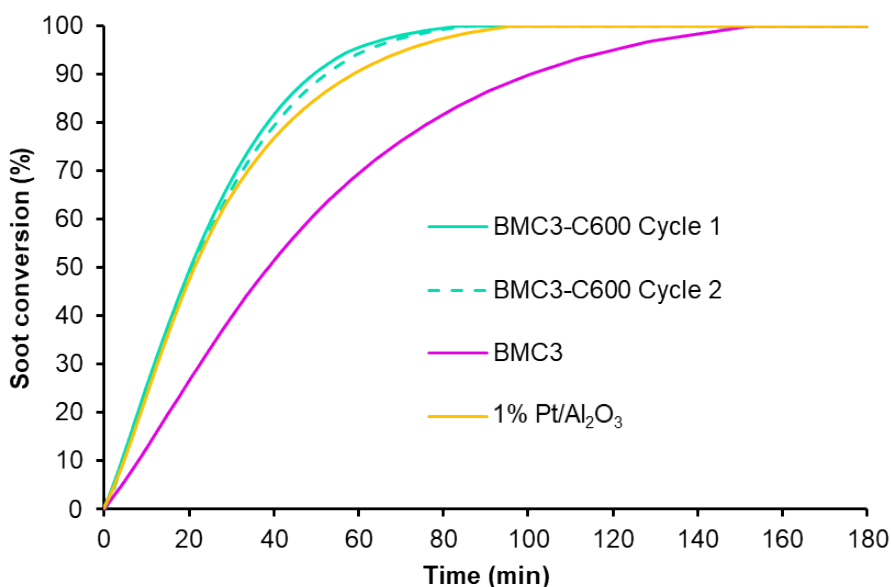experiment) and the CO_2 selectivity values are included. 493

494

Figure 14. Soot conversion profiles at 450ºC for BMC3-C600 and BMC3 and 495
1%Pt/Al_2O_3 as references 496

The soot conversion profiles in isothermal conditions for first cycle features that, during the first 20 minutes, BMC3-C600 and the platinum-based catalyst show a similar catalytic performance, therefore, both catalysts show similar initial soot oxidation rates (see Table 4). Moreover, during the second cycle, BMC3-C600 catalyst keeps the catalytic activity, so, it seems that the reaction conditions allow the regeneration of the catalyst [73, 79]. Finally, at 450ºC, the CO_2 selectivity is over 90%, and it remains during the second soot oxidation cycle.

Table 4. Initial soot oxidation rates at 450ºC and CO_2 selectivity for BMC3-C600 series, and BMC3 and 1%Pt/Al$_2$O$_3$ as references. The data for the second consecutive cycle is included in brackets

	Initial soot oxidation rate (10^{-2} mmol/min)	CO_2 selectivity (%)
BMC3-C600	3.3 (3.4)	89 (90)
BMC3	2.2	97
1%Pt/Al$_2$O$_3$	2.7	100

As a final remark, the performance of the best catalysts of the BM-CX series (BM-C700) [25] and the BMC3-CX series (BMC3-C600) has been compared in order to understand the role of copper. Both catalysts show similar T50% value (490ºC) and initial soot oxidation rate after two successive isothermal reaction cycles at 450ºC (3.3 10^{-2} mmol/min). So, it seems that copper is not able to further improve the catalytic behaviour shown by BM-C700, obtained using carbon black during sol-gel synthesis. In fact, the unique advantage of using copper in the modified sol-gel synthesis is an additional decrease of 100ºC in the calcination temperature used for the synthesis of the best catalyst, which is 700ºC for BM-CX and 600ºC for BMC3-CX.

3.3. Characterization of used catalysts

The catalysts used in the activity tests (NO$_x$-TPR and isothermal soot oxidation) have been characterized by XRD and XPS in order to check if the samples are modified during reactions.

Figures 15 and 16 compare the X-Ray patterns of fresh catalysts and of catalysts used in three successive NO$_x$-TPR cycles. Used BMC3-C600 shows a lower amount of barium carbonate because NO$_x$-TPR conditions allow its removal. Also, it seems that the NO$_x$-TPR conditions promote the formation of the BaMnO$_3$ polytype phase and, after three cycles, a mixture of BaMnO$_3$ hexagonal perovskite and the BaMnO$_3$ polytype phases are detected. BMC3-C700 shows similar changes that BMC3-600, barium carbonate is removed and BaMnO$_3$ polytype phase is enhanced in detriment

of the hexagonal perovskite phase. However, no crystallinity changes are detected   529

in used BMC3-C750. In conclusion, NO_x-TPR conditions promote some structural   530

modifications for the catalysts calcined at temperatures below 750ºC, removing   531

barium carbonate and promoting the $BaMnO_3$ polytype formation in detriment of   532
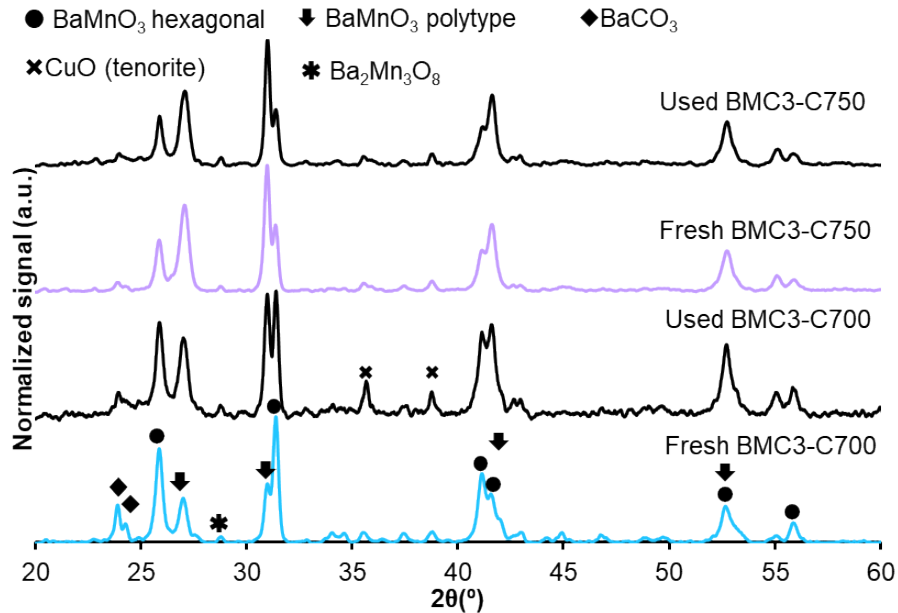
the perovskite hexagonal phase.   533

Figure 15. X-Ray patterns for fresh and used BMC3-C700 and BMC3-C750 catalysts,   534
after three NO_x-TPR consecutive cycles   535

Figure 16. X-Ray patterns for fresh and used BMC3-C600 catalyst after three NO_x-   536
TPR consecutive cycles and after two isothermal soot oxidation cycles at 450ºC   537

On the other hand, Figure 16 shows the XRD patterns of BMC3-C600 catalysts   538

after two isothermal soot oxidation cycles at 450ºC, compared to the XRD patterns of   539

the fresh sample. Note that after reaction at 450ºC, BMC3-C600 presents almost the   540

same crystalline phases than the fresh catalyst. This finding confirms that the   541

formation of $BaMnO_3$ polytype requires high temperatures.   542

The XPS data for used samples reveal some changes in surface composition.   543

Table 5 features the Cu/Ba+Mn+Cu, $O_{Lattice}$/Ba+Mn+Cu and Mn(IV)/Mn(III) XPS   544
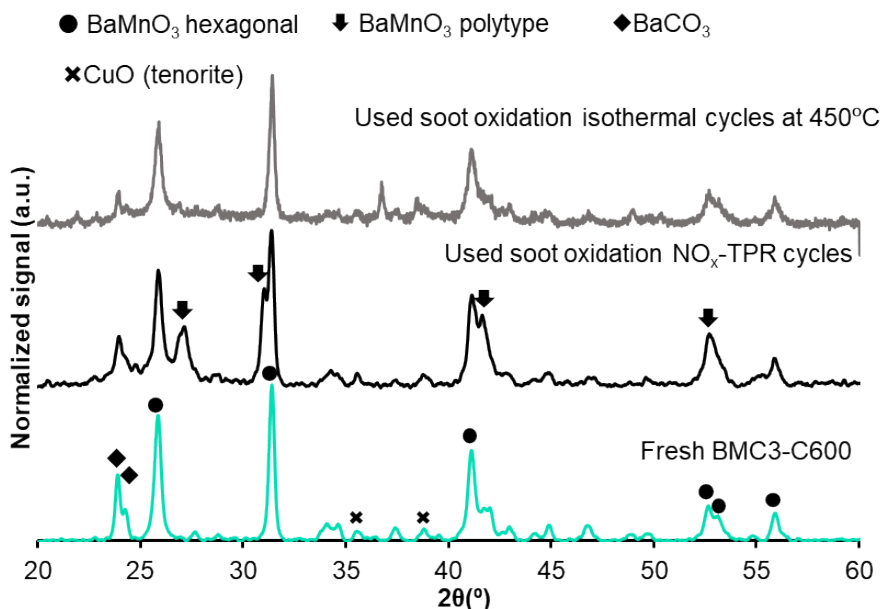
ratios for used and fresh catalysts. After NO$_x$-TPR experiments, BMC3-C600 shows a higher Cu/Ba+Mn+Cu ratio, i.e., the presence of copper increases on surface and a larger amount of surface oxygen vacancies, since the O$_{Lattice}$/Ba+Mn+Cu ratio decreases. The increase in the surface copper and in the number of oxygen vacancies seem to justify the higher activity and stability of BMC3-C600 after three consecutive NO$_x$-TPR cycles. Therefore, XPS data points out the amount of surface copper and oxygen vacancies as key factors for the soot oxidation process.

Table 5. XPS ratios for fresh and BMC3-CX catalysts used in successive NOx-TPR and isothermal cycles (data in brackets)

	Cu/(Mn+Ba+Cu)		O$_{Lattice}$/(Mn+Ba+Cu)		Mn(IV)/Mn(III)	
	Used	Fresh	Used	Fresh	Used	Fresh
BMC3-C600	0.19 (0.13)	0.15	0.5 (0.8)	1.0	0.8 (0.8)	0.9
BMC3-C700	0.09	0.13	0.6	1.1	0.6	0.6
BMC3-C750	0.13	0.13	0.6	1.0	0.6	0.5

On the contrary, after two cycles of soot oxidation at 450ºC (data in brackets), the surface chemical composition does not significantly differ from the corresponding to fresh BMC3-C600. Therefore, it seems that BMC3-C600 is stable during successive isothermal experiments at 450ºC as the used conditions do not modify the surface chemical properties during the experiment.

For used BMC3-C700 an increase in the amount of surface oxygen vacancies is also detected, but the Cu/Ba+Mn+Cu ratio indicates a decrease in the amount of surface copper respect to fresh sample, therefore the used BMC3-C700 is less active than the fresh one. A similar effect is observed for BMC3-C750 used catalyst, which presents a higher amount of oxygen vacancies, but the surface copper ratio is not modified.

Finally, no significant changes in Mn(IV)/Mn(III) surface ratio are detected for any of used catalysts, so , the Mn(IV)/Mn(III) redox pair is not modified during activity tests.

In conclusion, the characterization results for used catalysts indicate that a combination of a high amount of surface copper and oxygen vacancies seems to be needed to achieve an active and stable catalyst for NO$_x$-assisted soot oxidation. BMC3-C600 presents the best performance as it features a high amount of surface copper and oxygen vacancies that increase during reaction. However, as the amount

of surface copper does not increase for the samples calcined at temperatures higher than 600ºC, the catalysts become less active and stable.

4. Conclusions

$BaMn_{0.7}Cu_{0.3}O_3$ catalysts series (BMC3-CX) have been synthesized by a modified sol-gel method. The characterization and activity results suggest the following statements:

The use of a carbon black during sol-gel synthesis of BMC3 mixed oxide allows to diminish the calcination temperature to achieve the perovskite structure, but it hinders the formation of $BaMnO_3$ polytype, which is the unique crystal phase identified for BMC3 reference obtained by the conventional sol-gel synthesis, i.e., in the absence of carbon black.

Low calcination temperatures reduce the sintering effects, obtaining mixed oxides with lower particle size, slightly higher BET surface areas and macropores with lower diameter than BMC3.

The distribution of copper in BMC3-CX catalysts depends on the calcination temperature, as it is deduced by H_2-TPR and XPS data. Copper insertion into the perovskite structure is promoted as the calcination temperature increases and, consequently, the $BaMnO_3$ polytype structure is formed, being the main crystal phase at calcination temperatures above 850ºC.

All BMC3-CX catalysts are active for NO to NO_2 and NO_x-assisted soot oxidation processes, but only BMC3-C600 and BMC3-C700 show higher catalytic activity than BMC3 reference.

BMC3-C600 shows the most stable performance during cyclic NO_x-TPR experiments, being even better than the featured by BMC3. The characterization of used catalysts points out that the easier diffusion of copper to the surface, and the increase in the amount of oxygen surface vacancies, which are active sites for the oxidation process under study, seem to justify the improved catalytic performance.

The characterization of used BMC3-C600 reveals that it shows a stable performance during successive isothermal soot oxidation at 450ºC because the chemical properties of the catalyst are not significantly modified during reaction.

The comparison of the catalytic performance of BMC3-C600 with the best catalyst of BM-CX series (BM-C700) reveals that the unique advantage of using copper in the modified sol-gel synthesis is an additional decrease of 100ºC in the calcination temperature required for the synthesis of the best catalyst, which is 700ºC for BM-CX and 600ºC for BMC3-CX.

Apendix A

The weight percentage and CO_2 emission profiles for BMC3-CX series, plotted in Figure A.1, reveal that the calcination temperatures used allow the efficient removal of almost all the carbon black. In fact, the percentage of remaining carbon black, calculated based on the CO_2 evolved during TGA experiments (Figure A1.b) and included in Table A.1, is lower as calcination temperature increases, ranging from 6% in BMC3-C600 up to 1%.
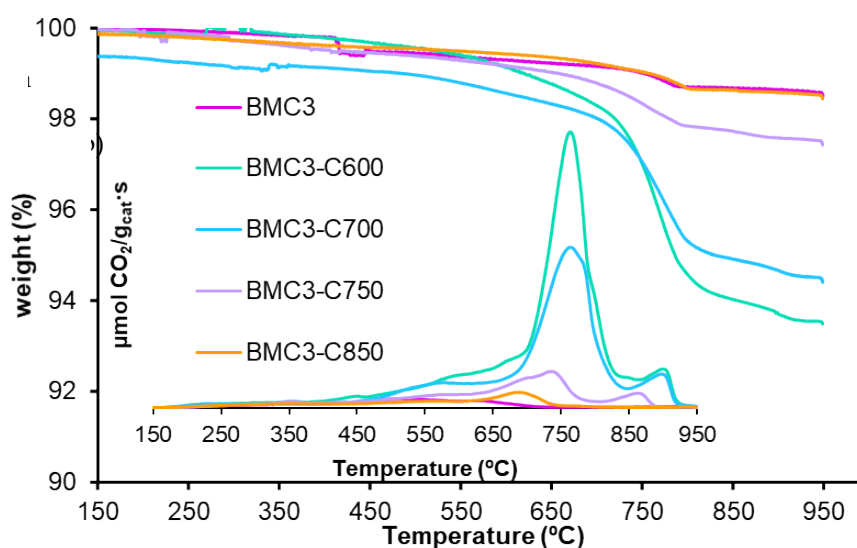

Figure A.1. (a) TGA profiles and (b) 44 m/z MS signal for BMC3-CX series and BMC3 as reference.

Table A 1. Total weight loss calculated by TG and MS data for BMC3-CX series and BMC3 as reference.

	Weight loss (TG) (%)	Weight loss (MS, CO_2, m/z= 44 (%)
BMC3-C600	7	6
BMC3-C700	6	4
BMC3-C750	3	2
BMC3-C850	2	1
BMC3	2	0

References

[1] Bhalla, A. S. S.; Guo, R.; Roy, R. The Perovskite Structure - a Review of Its Role in Ceramic Science and Technology. *Mater. Res. Innov.* 2000, *4* (1), 3–26. https://doi.org/10.1007/s100190000062.

[2] Peña, M. A.; Fierro, J. L. G. Chemical Structures and Performance of Perovskite Oxides. *Chem. Rev.* **2001**, *101* (7), 1981–2017. https://doi.org/10.1021/cr980129f.

[3] Royer, S.; Duprez, D.; Can, F.; Courtois, X.; Batiot-Dupeyrat, C.; Laassiri, S.; Alamdari, H. Perovskites as Substitutes of Noble Metals for Heterogeneous Catalysis: Dream or Reality. *Chem. Rev.* **2014**, *114* (20), 10292–10368. https://doi.org/10.1021/cr500032a.

[4] Nair, M. M.; Kaliaguine, S. Synthesis and Catalytic Applications of Nanocast Oxide-Type Perovskites. In *Perovskites and Related Mixed Oxides: Concepts and Applications*; Granger, P., Parvulescu, V. I., Kaliagne, S., Prellier, W., Eds.; Wiley-VCH Verlag GmbH & Co. KGaA: Weinheim, Germany, 2016; pp 47–68. https://doi.org/10.1002/9783527686605.ch03.

[5] Miniajluk, N.; Trawczyński, J.; Zawadzki, M.; Tomaszewski, P. E.; Miśta, W. Solvothermal Synthesis and Characterization of Mixed Oxides with Perovskite-like Structure. *Catal. Today* **2015**, *257*, 26–34. https://doi.org/10.1016/j.cattod.2015.03.029.

[6] Athayde, D. D.; Souza, D. F.; Silva, A. M. A.; Vasconcelos, D.; Nunes, E. H. M.; Diniz da Costa, J. C.; Vasconcelos, W. L. Review of Perovskite Ceramic Synthesis and Membrane Preparation Methods. *Ceram. Int.* **2016**, *42*, 6555–6571. https://doi.org/10.1016/j.ceramint.2016.01.130.

[7] Chen, A.; Zhi, Y.; Zhi, J.; Vilarinho, P. M.; Baptista, J. L. Synthesis and Characterization Ceramics. **1997**, *2219* (96), 2–6.

[8] Modeshia, D. R.; Walton, R. I. Solvothermal Synthesis of Perovskites and Pyrochlores: Crystallisation of Functional Oxides under Mild Conditions. *Chem. Soc. Rev.* **2010**, *39* (11), 4303. https://doi.org/10.1039/b904702f.

[9] Afzal, S.; Quan, X.; Zhang, J. High Surface Area Mesoporous Nanocast $LaMO_3$ (M = Mn, Fe) Perovskites for Efficient Catalytic Ozonation and an Insight into Probable Catalytic Mechanism. *Appl. Catal. B Environ.* **2017**, *206*, 692–703. https://doi.org/10.1016/j.apcatb.2017.01.072.

[10] Chen, J.; Shen, M.; Wang, X.; Wang, J.; Su, Y.; Zhao, Z. Catalytic Performance of NO Oxidation over $LaMeO_3$ (Me=Mn, Fe, Co) Perovskite Prepared by the Sol–Gel Method. *Catal. Commun.* **2013**, *37*, 105–108. https://doi.org/10.1016/j.catcom.2013.03.039.

[11] Yoon, D. Y.; Lim, E.; Kim, Y. J.; Kim, J. H.; Ryu, T.; Lee, S.; Cho, B. K.; Nam, I.-S.; Choung, J. W.; Yoo, S. NO Oxidation Activity of Ag-Doped Perovskite Catalysts. *J. Catal.* **2014**, *319*, 182–193. https://doi.org/10.1016/j.jcat.2014.09.007.

[12] Wang, H.; Zhao, Z.; Xu, C. M.; Liu, J. Nanometric $La_{1-x} K_xMnO_3$ Perovskite-Type Oxides - Highly Active Catalysts for the Combustion of Diesel Soot Particle under Loose Contact Conditions. *Catal. Letters* **2005**, *102* (3–4), 251–256. https://doi.org/10.1007/s10562-005-5864-4.

[13] Rojas, M. L. L.; Fierro, J. L. . G.; Tejuca, L. G. G.; Bell, T. A.; Bell, A. T. Preparation and Characterization of $LaMn_{1-x}Cu_xO_3$ Perovskite Oxides. *J. Catal.* **1990**, *124* (1), 41–51. https://doi.org/10.1016/0021-9517(90)90102-P.

[14] Albaladejo-Fuentes, V.; López-Suárez, F. E.; Sánchez-Adsuar, M. S.; Illán-Gómez, M. J. Tailoring the Properties of $BaTi_{0.8}Cu_{0.2}O_3$ Catalyst Selecting the Synthesis Method. *Appl. Catal. A Gen.* **2016**, *519*, 7–15. https://doi.org/10.1016/j.apcata.2016.03.022.

[15] Agüero, F. N.; Morales, M. R.; Larrégola, S.; Izurieta, E. M.; Lopez, E.; Cadús, L. E. $La_{1-x}Ca_xAl_{1-Y}Ni_yO_3$ Perovskites Used as Precursors of Nickel Based Catalysts for Ethanol

Steam Reforming. *Int. J. Hydrogen Energy* **2015**, *40* (45), 15510–15520. 671
https://doi.org/10.1016/j.ijhydene.2015.08.051. 672

[16] Tanaka, H.; Mizuno, N.; Misono, M. Catalytic Activity and Structural Stability of 673
$La_{0.9}Ce_{0.1}Co_{1-x}Fe_xO_3$ Perovskite Catalysts for Automotive Emissions Control. *Appl. Catal.* 674
A Gen. **2003**, *244* (2), 371–382. https://doi.org/10.1016/S0926-860X(02)00609-9. 675

[17] Tarjomannejad, A.; Niaei, A.; Farzi, A.; Salari, D.; Zonouz, P. R. Catalytic Oxidation of 676
CO over $LaMn_{1-x}B_xO_3$ (B = Cu, Fe) Perovskite-Type Oxides. *Catal. Letters* **2016**, *146* (8), 677
1544–1551. https://doi.org/10.1007/s10562-016-1788-4. 678

[18] Ge, C.; Li, L.; Xian, H.; Yan, H.; Meng, M.; Li, X. Effects of Ti-Doping on the NO_x Storage 679
and the Sulfur Resistance of the $BaFe_{1-x}Ti_xO_{3-y}$ Perovskite-Type Catalysts for Lean-Burn 680
Exhausts. *Fuel Process. Technol.* **2014**, *120*, 1–7. https://doi.org/10.1016/j.fuproc.2013.11.008. 681

[19] Liu, J.-B.; Li, W.-C.; Wang, Z.-M.; Zheng, C.-P. Preparation and Characterisation of 682
Lanthanum Doped $BaTiO_3$ Nanosize Polycrystals by Sol–Gel Processing. *Mater. Sci.* 683
Technol. **2001**, *17* (5), 606–608. https://doi.org/10.1179/026708301101510302. 684

[20] Zhan, H.; Li, F.; Gao, P.; Zhao, N.; Xiao, F.; Wei, W.; Sun, Y. Influence of Element Doping 685
on La–Mn–Cu–O Based Perovskite Precursors for Methanol Synthesis from CO_2/H_2. *RSC* 686
Adv. **2014**, *4* (90), 48888–48896. https://doi.org/10.1039/C4RA07692C. 687

[21] Johnson, T. V. Diesel Emission Control in Review. In *SAE Paper 2009-01-0121*; 2009; Vol. 688
2, pp 1–12. https://doi.org/10.4271/2006-01-0030. 689

[22] Keav, S.; Matam, S.; Ferri, D.; Weidenkaff, A. Structured Perovskite-Based Catalysts and 690
Their Application as Three-Way Catalytic Converters—A Review. *Catalysts* **2014**, *4* (3), 691
226–255. https://doi.org/10.3390/catal4030226. 692

[23] Guan, B.; Zhan, R.; Lin, H.; Huang, Z. Review of State of the Art Technologies of 693
Selective Catalytic Reduction of NO_x from Diesel Engine Exhaust. *Appl. Therm. Eng.* **2014**, 694
66, 395–414. https://doi.org/10.1016/j.applthermaleng.2014.02.021. 695

[24] Mishra, A.; Prasad, R. Preparation and Application of Perovskite Catalysts for Diesel 696
Soot Emissions Control: An Overview. *Catal. Rev.* **2014**, *56* (1), 57–81. 697
https://doi.org/10.1080/01614940.2014.866438. 698

[25] Torregrosa-Rivero, Sánchez-Adsuar, M.S.; Illán-Gómez, M.J., Improving the performance 699
of $BaMnO_3$ perovskite as soot oxidation catalyst using carbon black during sol-gel 700
synthesis. *Nanomaterials, under review.* 701

[26] Torregrosa-Rivero, V.; Albaladejo-Fuentes, V.; Sánchez-Adsuar, M.S.; Illán-Gómez, M.J. 702
Copper Doped $BaMnO_3$ Perovskite Catalysts for NO Oxidation and NO_2 -Assisted Diesel 703
Soot Removal. *RSC Adv.* **2017**, *7* (56), 35228–35238. https://doi.org/10.1039/C7RA04980C. 704

[27] Atkins, P. W.; Overton, T.; Rourke, J.; Weller, M.; Armstrong, F.; Hagerman, M. *Shriver &* 705
Atkins' Inorganic Chemistry, 5th ed.; W.H. Freeman and Company, Ed.; Oxford University 706
Press, 2010. https://doi.org/978-0-19-926463-6. 707

[28] Albaladejo-Fuentes, V.; López-Suárez, F.; Sánchez-Adsuar, M. S.; Illán-Gómez, M. J. 708
$BaTi_{0.8}Cu_{0.2}O_3$ Catalysts for NO Oxidation and NO_x Storage: Effect of Synthesis Method. 709
Top. Catal. **2017**, *60* (3–5), 220–224. https://doi.org/10.1007/s11244-016-0601-3. 710

[29] Ma, A. J.; Wang, S. Z.; Liu, C.; Xian, H.; Ding, Q.; Guo, L.; Meng, M.; Tan, Y. S.; Tsubaki, 711
N.; Zhang, J.; Zheng, L. R.; Li, X. G. Effects of Fe Dopants and Residual Carbonates on the 712
Catalytic Activities of the Perovskite-Type $La_{0.7}Sr_{0.3}Co_{1-x}Fe_xO_3$ NO_x Storage Catalyst. *Appl.* 713
Catal. B Environ. **2014**, *146*, 24–34. https://doi.org/10.1016/j.apcatb.2013.06.005. 714

[30] Civera, A.; Pavese, M.; Saracco, G.; Specchia, V. Combustion Synthesis of Perovskite- 715
Type Catalysts for Natural Gas Combustion. *Catal. Today* **2003**, *83* (1–4), 199–211. 716
https://doi.org/10.1016/S0920-5861(03)00220-7. 717

[31] Wang, L.; Fang, S.; Feng, N.; Wan, H.; Guan, G. Efficient Catalytic Removal of Diesel Soot 718
over Mg Substituted K/La$_{0.8}$Ce$_{0.2}$CoO$_3$ Perovskites with Large Surface Areas. *Chem. Eng. J.* 719
2016, *293*, 68–74. https://doi.org/10.1016/j.cej.2016.02.038. 720

[32] Sun, S.; Yang, L.; Pang, G.; Feng, S. Surface Properties of Mg Doped LaCoO$_3$ Particles 721
with Large Surface Areas and Their Enhanced Catalytic Activity for CO Oxidation. *Appl.* 722
Catal. A Gen. **2011**, *401* (1–2), 199–203. https://doi.org/10.1016/j.apcata.2011.05.015. 723

[33] Labhasetwar, N.; Saravanan, G.; Kumar-Megarajan, S.; Manwar, N.; Khobragade, R.; 724
Doggali, P.; Grasset, F. Perovskite-Type Catalytic Materials for Environmental 725
Applications. *Sci. Technol. Adv. Mater.* **2015**, *16* (3), 1–13. https://doi.org/10.1088/1468- 726
6996/16/3/036002. 727

[34] Lisi, L.; Bagnasco, G.; Ciambelli, P.; De Rossi, S.; Porta, P.; Russo, G.; Turco, M. 728
Perovskite-Type Oxides II. Redox Properties of LaMn$_{1-x}$Cu$_x$O$_3$ and LaCo$_{1-x}$Cu$_x$O$_3$ and 729
Methane Catalytic Combustion. *J. Solid State Chem.* **1999**, *146* (1), 176–183. 730
https://doi.org/10.1006/jssc.1999.8327. 731

[35] Najjar, H.; Batis, H. Development of Mn-Based Perovskite Materials: Chemical Structure 732
and Applications. *Catal. Rev.* **2016**, *58* (3), 371–438. 733
https://doi.org/10.1080/01614940.2016.1198203. 734

[36] Sadakane, M.; Horiuchi, T.; Kato, N.; Sasaki, K.; Ueda, W. Preparation of Three- 735
Dimensionally Ordered Macroporous Perovskite-Type Lanthanum-Iron-Oxide LaFeO$_3$ 736
with Tunable Pore Diameters: High Porosity and Photonic Property. *J. Solid State Chem.* 737
2010, *183* (6), 1365–1371. https://doi.org/10.1016/j.jssc.2010.04.012. 738

[37] Alcalde-Santiago, V.; Davó-Quiñonero, A.; Such-Basáñez, I.; Lozano-Castelló, D.; Bueno- 739
López, A. Macroporous Carrier-Free Sr-Ti Catalyst for NO$_x$ Storage and Reduction. *Appl.* 740
Catal. B Environ. **2018**, *220* (May 2017), 524–532. 741
https://doi.org/10.1016/j.apcatb.2017.08.062. 742

[38] Monte, M.; Munuera, G.; Costa, D.; Conesa, J. C.; Martínez-Arias, A. Near-Ambient XPS 743
Characterization of Interfacial Copper Species in Ceria-Supported Copper Catalysts. 744
Phys. Chem. Chem. Phys. **2015**, *17* (44), 29995–30004. https://doi.org/10.1039/c5cp04354a. 745

[39] Moulder, J. F.; Stickle, W. F.; Sobol, P. E.; Bomben, K. D. Handbook of X-Ray 746
Photoelectron Spectroscopy : A Reference Book of Standard Spectra for Identification and 747
Interpretation of XPS Data; Chastain, J., Ed.; Perkin-Elmer Corporation, Physical 748
Electronic Division: Eden Praire, Minnesota, 1992. 749

[40] Naumkin, A. V.; Anna Kraut-Kraut-Vass, A.; Gaarenstroom, S. W.; Powell, C. J. NIST X- 750
ray Photoelectron Spectroscopy Database 20, Version 4.1 https://srdata.nist.gov/xps/. 751
https://doi.org/http://dx.doi.org/10.18434/T4T88K. 752

[41] López-Suárez, F. E.; Bueno-López, A.; Illán-Gómez, M. J.; Adamski, A.; Ura, B.; 753
Trawczynski, J. Copper Catalysts for Soot Oxidation: Alumina versus Perovskite 754
Supports. *Environ. Sci. Technol.* **2008**, *42* (20), 7670–7675. https://doi.org/10.1021/es8009293. 755

[42] López-Suárez, F. E.; Parres-Esclapez, S.; Bueno-López, A.; Illán-Gómez, M. J.; Ura, B.; 756
Trawczynski, J. Role of Surface and Lattice Copper Species in Copper-Containing 757
(Mg/Sr)TiO$_3$ Perovskite Catalysts for Soot Combustion. *Appl. Catal. B Environ.* **2009**, *93* (1– 758
2), 82–89. https://doi.org/10.1016/j.apcatb.2009.09.015. 759

[43] Oku, M.; Hirokawa, K.; Ikeda, S. X-Ray Photoelectron Spectroscopy of Manganese-Oxygen Systems. *J. Electron Spectros. Relat. Phenomena* **1975**, *7* (5), 465–473. https://doi.org/10.1016/0368-2048(75)85010-9.

[44] Abdulhamid, H.; Dawody, J.; Fridell, E.; Skoglundh, M. A Combined Transient in Situ FTIR and Flow Reactor Study of NO_x Storage and Reduction over $M/BaCO_3/Al_2O_3$ (M = Pt, Pd or Rh) Catalysts. *J. Catal.* **2006**, *244* (2), 169–182. https://doi.org/10.1016/j.jcat.2006.09.003.

[45] Najjar, H.; Lamonier, J. F.; Mentré, O.; Giraudon, J. M.; Batis, H. Optimization of the Combustion Synthesis towards Efficient $LaMnO_{3+y}$ Catalysts in Methane Oxidation. *Appl. Catal. B Environ.* **2011**, *106* (1–2), 149–159. https://doi.org/10.1016/j.apcatb.2011.05.019.

[46] Najjar, H.; Batis, H. La–Mn Perovskite-Type Oxide Prepared by Combustion Method: Catalytic Activity in Ethanol Oxidation. *Appl. Catal. A Gen.* **2010**, *383* (1–2), 192–201. https://doi.org/10.1016/j.apcata.2010.05.048.

[47] Merino, N. A.; Barbero, B. P.; Eloy, P.; Cadús, L. E. $La_{1-x}Ca_xCoO_3$ Perovskite-Type Oxides: Identification of the Surface Oxygen Species by XPS. *Appl. Surf. Sci.* **2006**, *253* (3), 1489–1493. https://doi.org/10.1016/j.apsusc.2006.02.035.

[48] Niu, J.; Deng, J.; Liu, W.; Zhang, L.; Wang, G.; Dai, H.; He, H.; Zi, X. Nanosized Perovskite-Type Oxides $La_{1-x}Sr_xMO_{3-\delta}$ (M = Co, Mn; x = 0, 0.4) for the Catalytic Removal of Ethylacetate. *Catal. Today* **2007**, *126* (3–4), 420–429. https://doi.org/10.1016/j.cattod.2007.06.027.

[49] Esmaeilnejad-Ahranjani, P.; Khodadadi, A.; Ziaei-Azad, H.; Mortazavi, Y. Effects of Excess Manganese in Lanthanum Manganite Perovskite on Lowering Oxidation Light-off Temperature for Automotive Exhaust Gas Pollutants. *Chem. Eng. J.* 2011, pp 282–289. https://doi.org/10.1016/j.cej.2011.02.062.

[50] Chen, J.; Shen, M.; Wang, X.; Qi, G.; Wang, J.; Li, W. The Influence of Nonstoichiometry on $LaMnO_3$ Perovskite for Catalytic NO Oxidation. *Appl. Catal. B Environ.* **2013**, *134–135*, 251–257. https://doi.org/10.1016/j.apcatb.2013.01.027.

[51] Irusta, S.; Pina, M. P.; Menéndez, M.; Santamaría, J. Catalytic Combustion of Volatile Organic Compounds over La-Based Perovskites. *J. Catal.* **1998**, *179* (2), 400–412. https://doi.org/10.1006/jcat.1998.2244.

[52] Gao, Y.; Wu, X.; Liu, S.; Weng, D.; Zhang, H.; Ran, R. Formation of $BaMnO_3$ in Ba/MnO_x–CeO_2 Catalyst upon the Hydrothermal Ageing and Its Effects on Oxide Sintering and Soot Oxidation Activity. *Catal. Today* **2015**, *253* (2), 83–88. https://doi.org/10.1016/j.cattod.2014.11.032.

[53] Royer, S.; Bérubé, F.; Kaliaguine, S. Effect of the Synthesis Conditions on the Redox and Catalytic Properties in Oxidation Reactions of $LaCo_{1-x}Fe_xO_3$. *Appl. Catal. A Gen.* **2005**, *282*, 273–284. https://doi.org/10.1016/j.apcata.2004.12.018.

[54] Patcas, F.; Buciuman, F. C.; Zsako, J. Oxygen Non-Stoichiometry and Reducibility of B-Site Substituted Lanthanum Manganites. *Thermochim. Acta* **2000**, *360* (1), 71–76. https://doi.org/10.1016/S0040-6031(00)00532-3.

[55] Lisi, L.; Bagnasco, G.; Ciambelli, P.; De Rossi, S.; Porta, P.; Russo, G.; Turco, M. Perovskite-Type Oxides II. Redox Properties of $LaMn_{1-x}Cu_xO_3$ and $LaCo_{1-x}Cu_xO_3$ and Methane Catalytic Combustion. *J. Solid State Chem.* **1999**, *146* (1), 176–183. https://doi.org/10.1006/jssc.1999.8327.

[56] Zhang, C.; Wang, C.; Hua, W.; Guo, Y.; Lu, G.; Gil, S.; Giroir-Fendler, A. Relationship between Catalytic Deactivation and Physicochemical Properties of $LaMnO_3$ Perovskite

Catalyst during Catalytic Oxidation of Vinyl Chloride. *Appl. Catal. B Environ.* **2016**, *186*, 173–183. https://doi.org/10.1016/j.apcatb.2015.12.052.

[57] Rojas, M. L.; Fierro, J. L. G.; Tejuca, L. G.; Bell, T. A. Preparation and Characterization of $LaMn_{1-x}Cu_xO_{3+\delta}$ Perovskite Oxides. *J. Catal.* **1990**, *124* (1), 41–51. https://doi.org/10.1016/0021-9517(90)90102-P.

[58] Tien-Thao, N.; Alamdari, H.; Zahedi-Niaki, M. H. H.; Kaliaguine, S. $LaCo_{1-x}Cu_xO_{3-\delta}$ Perovskite Catalysts for Higher Alcohol Synthesis. *Appl. Catal. A Gen.* **2006**, *311* (1–2), 204–212. https://doi.org/10.1016/j.apcata.2006.06.029.

[59] Peron, G.; Glisenti, A. Perovskites as Alternatives to Noble Metals in Automotive Exhaust Abatement: Activation of Oxygen on $LaCrO_3$ and $LaMnO_3$. *Top. Catal.* **2019**, *62* (1–4), 244–251. https://doi.org/10.1007/s11244-018-1120-1.

[60] Levasseur, B.; Kaliaguine, S. Effect of the Rare Earth in the Perovskite-Type Mixed Oxides $AMnO_3$ (A=Y, La, Pr, Sm, Dy) as Catalysts in Methanol Oxidation. *J. Solid State Chem.* **2008**, *181* (11), 2953–2963. https://doi.org/10.1016/j.jssc.2008.07.029.

[61] Zhu, H.; Zhang, P.; Dai, S. Recent Advances of Lanthanum-Based Perovskite Oxides for Catalysis. *ACS Catal.* **2015**, *5* (11), 6370–6385. https://doi.org/10.1021/acscatal.5b01667.

[62] Dong, Y. H.; Xian, H.; Lv, J. L.; Liu, C.; Guo, L.; Meng, M.; Tan, Y. S.; Tsubaki, N.; Li, X. G. Influence of Synthesis Conditions on NO Oxidation and NO_x Storage Performances of $La_{0.7}Sr_{0.3}MnO_3$ Perovskite-Type Catalyst in Lean-Burn Atmospheres. *Mater. Chem. Phys.* **2014**, *143* (2), 578–586. https://doi.org/10.1016/j.matchemphys.2013.09.035.

[63] Albaladejo-Fuentes, V.; Sánchez-Adsuar, M. S.; Illán-Gómez, M. J. Tolerance and Regeneration versus SO_2 of $Ba_{0.9}A_{0.1}Ti_{0.8}Cu_{0.2}O_3$ (A = Sr, Ca, Mg) LNT Catalysts. *Appl. Catal. A Gen.* **2019**, *577*, 113–123. https://doi.org/10.1016/j.apcata.2019.03.023.

[64] Albaladejo-Fuentes, V.; López-Suárez, F. E.; Sánchez-Adsuar, M. S.; Illán-Gómez, M. J. $BaTi_{1-x}Cu_xO_3$ Perovskites: The Effect of Copper Content in the Properties and in the NOx Storage Capacity. *Appl. Catal. A Gen.* **2014**, *488*, 189–199. https://doi.org/10.1016/j.apcata.2014.09.032.

[65] Xian, H.; Zhang, X.; Li, X.; Zou, H.; Meng, M.; Zou, Z.; Guo, L.; Tsubaki, N. Effect of the Calcination Conditions on the NO_x Storage Behavior of the Perovskite $BaFeO_{3-x}$ Catalysts. *Catal. Today* **2010**, *158* (3–4), 215–219. https://doi.org/10.1016/j.cattod.2010.03.026.

[66] Onrubia-Calvo, J. A.; Pereda-Ayo, B.; González-Velasco, J. R. Perovskite-Based Catalysts as Efficient, Durable, and Economical NOx Storage and Reduction Systems. *Catalysts* **2020**, *10* (2). https://doi.org/10.3390/catal10020208.

[67] Le Phuc, N.; Courtois, X.; Can, F.; Royer, S.; Marecot, P.; Duprez, D. NOx Removal Efficiency and Ammonia Selectivity during the NO_x Storage-Reduction Process over $Pt/BaO(Fe, Mn, Ce)/Al_2O_3$ Model Catalysts. Part I: Influence of Fe and Mn Addition. *Appl. Catal. B Environ.* **2011**, *102* (3–4), 353–361. https://doi.org/10.1016/j.apcatb.2010.12.040.

[68] Milt, V. G.; Querini, C. A.; Miró, E. E.; Ulla, M. A. Abatement of Diesel Exhaust Pollutants: NOx Adsorption on $Co,Ba,K/CeO_2$ Catalysts. *J. Catal.* **2003**, *220* (2), 424–432. https://doi.org/10.1016/S0021-9517(03)00285-9.

[69] Dupré, J.; Bazin, P.; Marie, O.; Daturi, M.; Jeandel, X.; Meunier, F. Understanding the Storage Function of a Commercial NO_x-Storage-Reduction Material Using Operando IR under Realistic Conditions. *Appl. Catal. B Environ.* **2014**, *160–161* (1), 335–343. https://doi.org/10.1016/j.apcatb.2014.05.027.

806
807
808
809
810
811
812
813
814
815
816
817
818
819
820
821
822
823
824
825
826
827
828
829
830
831
832
833
834
835
836
837
838
839
840
841
842
843
844
845
846
847
848
849

[70] Roy, S.; Baiker, A. NO$_x$ Storage - Reduction Catalysis : From Mechanism and Materials Properties to Storage - Reduction Performance. *Chem. Rev.* **2008**, *109*, 4054–4091. https://doi.org/10.1021/cr800496f.

[71] Nejar, N.; Illán-Gómez, M. J. Performance of Potassium-Promoted Catalysts for NO$_x$ and Soot Removal from Simulated Diesel Exhaust. *Top. Catal.* **2007**, *42–43* (1–4), 277–282. https://doi.org/10.1007/s11244-007-0191-1.

Guilhaume, N.; Primet, M. Three-Way Catalytic Activity and Oxygen Storage Capacity of Perovskite LaMn$_{0.976}$Rh$_{0.024}$O$_{3+\delta}$. *J. Catal.* **1997**, *165* (2), 197–204. https://doi.org/10.1006/jcat.1997.1481.

[72] Esmaeilnejad-Ahranjani, P.; Khodadadi, A. A.; Mortazavi, Y. Self-Regenerative Function of Cu in LaMnCu$_{0.1}$O$_3$ Catalyst: Towards Noble Metal-Free Intelligent Perovskites for Automotive Exhaust Gas Treatment. *Applied Catalysis A: General*. 2020. https://doi.org/10.1016/j.apcata.2020.117702.

[73] Wiebenga, M. H.; Kim, C. H.; Schmieg, S. J.; Oh, S. H.; Brown, D. B.; Kim, D. H.; Lee, J.-H.; Peden, C. H. F. Deactivation Mechanisms of Pt/Pd-Based Diesel Oxidation Catalysts. *Catal. Today* **2012**, *184* (1), 197–204. https://doi.org/10.1016/j.cattod.2011.11.014.

[74] Uppara, H. P.; Pasuparthy, J. S.; Pradhan, S.; Singh, S. K.; Labhsetwar, N. K.; Dasari, H. The Comparative Experimental Investigations of SrMn(Co^{3+}/Co^{2+})O$_{3\pm\delta}$ and SrMn(Cu^{2+})O$_{3\pm\delta}$ Perovskites towards Soot Oxidation Activity. *Mol. Catal.* **2020**, *482*, 110665. https://doi.org/10.1016/j.mcat.2019.110665.

[75] Jin, B.; Zhao, B.; Liu, S.; Li, Z.; Li, K.; Ran, R.; Si, Z.; Weng, D.; Xiaodong, W. SmMn$_2$O$_5$ Catalysts Modified with Silver for Soot Oxidation: Dispersion of Silver and Distortion of Mullite. *Appl. Catal. B Environ.* **2020**, *273*. https://doi.org/10.1016/j.apcatb.2020.119058.

[76] Onrubia-Calvo, J. A.; Pereda-Ayo, B.; De-La-Torre, U.; González-Velasco, J. R. Key Factors in Sr-Doped LaBO$_3$ (B = Co or Mn) Perovskites for NO Oxidation in Efficient Diesel Exhaust Purification. *Appl. Catal. B Environ.* **2017**, *213* (1), 198–210. https://doi.org/10.1016/j.apcatb.2017.04.068.

[77] Urán, L.; Gallego, J.; Bailón-García, E.; Bueno-López, A.; Santamaría, A. Isotopic Study of the La$_{0.7}$Ag$_{0.3}$MnO$_{\delta\leq3}$ Perovskite-Catalyzed Soot Oxidation in Presence of NO. *Applied Catalysis A: General*. 2020. https://doi.org/10.1016/j.apcata.2020.117611.

[78] Tanaka, H.; Misono, M. Advances in Designing Perovskite Catalysts. *Curr. Opin. Solid State Mater. Sci.* **2001**, *5*, 381–387. https://doi.org/10.1016/S1359-0286(01)00035-3.